iScience

CellPress
OPEN ACCESS

Article

Reorganization of H3K9me heterochromatin leads to neuronal impairment via the cascading destruction of the KDM3B-centered epigenomic network

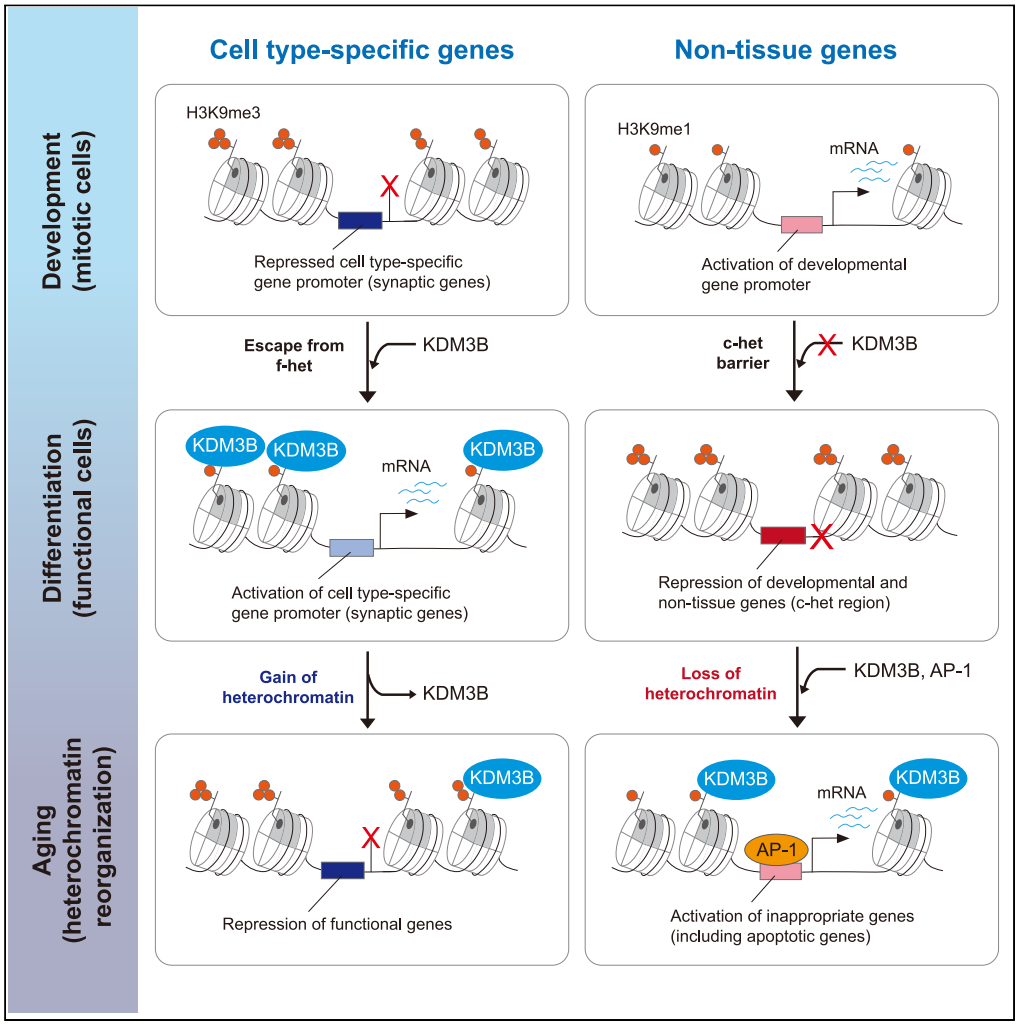

Mi-Jin An, Ji-Young Kim, Jinho Kim, ..., Sangmyung Rhee, Sang-Beom Seo, Jung-Woong Kim

jungkim@cau.ac.kr

Highlights

H3K9me heterochromatin is reorganized during the aging of cone photoreceptors

KDM3B regulates specific heterochromatin features of gene sets during retinal aging

Demethylase function of KDM3B controls apoptotic signaling and synaptic transmission

KDM3B-centered network is essential for balancing of gene regulation of cones

An et al., iScience 27, 110380
August 16, 2024
https://doi.org/10.1016/j.isci.2024.110380

iScience

CellPress
OPEN ACCESS

Article

Reorganization of H3K9me heterochromatin leads to neuronal impairment via the cascading destruction of the KDM3B-centered epigenomic network

Mi-Jin An,[1,2] Ji-Young Kim,[1,2] Jinho Kim,[1,2] Dae-Hyun Kim,[1] Geun-Seup Shin,[1] Hyun-Min Lee,[1] Ah-Ra Jo,[1] Yuna Park,[1] Yujeong Hwangbo,[1] Chul-Hong Kim,[1] Mi Jin Kim,[1] Youn-Sang Jung,[1] Jeongkyu Kim,[1] Sangmyung Rhee,[1] Sang-Beom Seo,[1] and Jung-Woong Kim[1,3,*]

SUMMARY

Histone H3K9 methylated heterochromatin silences repetitive non-coding sequences and lineage-specific genes during development, but how tissue-specific genes escape from heterochromatin in differentiated cells is unclear. Here, we examine age-dependent transcriptomic profiling of terminally differentiated mouse retina to identify epigenetic regulators involved in heterochromatin reorganization. The single-cell RNA sequencing analysis reveals a gradual downregulation of *Kdm3b* in cone photoreceptors during aging. Disruption of *Kdm3b* (*Kdm3b*$^{+/-}$) of 12-month-old mouse retina leads to the decreasing number of cones via apoptosis, and it changes the morphology of cone ribbon synapses. Integration of the transcriptome with epigenomic analysis in *Kdm3b*$^{+/-}$ retinas demonstrates gains of heterochromatin features in synapse assembly and vesicle transport genes that are downregulated via the accumulation of H3K9me1/2. Contrarily, losses of heterochromatin in apoptotic genes exacerbated retinal neurodegeneration. We propose that the KDM3B-centered epigenomic network is crucial for balancing of cone photoreceptor homeostasis via the modulation of gene set-specific heterochromatin features during aging.

INTRODUCTION

Cell identity establishment and maintenance critically rely on the precise control of gene expression, which is orchestrated by transcription factors and reinforced through a complex interplay of epigenetic mechanisms.[1] Among these mechanisms, heterochromatin formation plays a critical role in maintaining genomic instability and enabling the selective cell type-specific repression of genes.[2] Heterochromatin is composed of a functionally distinct chromosomal domain that is classically characterized by repressive histone modifications, such as H3K9me2/3 serving as a marker for constitutive heterochromatin and H3K27me3 indicating facultative heterochromatin.[3] Although recent research suggests that H3K9me1/2 in facultative heterochromatin has dynamic roles in repressing tissue-specific genes during early development,[4,5] it has yet to be revealed how these suppressed tissue-specific genes are reopened for the appropriate functional gene expressions in terminally differentiated cells.

Heterochromatin impedes the binding of transcription factors, effectively acting as a barrier that restricts gene activation and safeguards against changes in lineage commitment and cell identity.[6,7] Age-related destabilization of tightly compacted heterochromatin leads to aberrant gene expression followed by cellular dysfunction.[8] During the process of cellular differentiation, there is a crucial transition where cell type-specific genes experience a loss of heterochromatin, while lineage inappropriate genes undergo heterochromatin gain.[7] These established chromatin features of differentiated cells gradually disappear with aging, characterized by decreased heterochromatin maintenance markers.[9] For example, the expression levels of histone methyltransferase SUV39H1 in hematopoietic stem cells were decreased during aging, leading to a global decrease in H3K9me3 and disrupted heterochromatin function.[10] The double knockout of histone lysine methyltransferases (KMTs), MET-2 (SETDB1 homolog) and SET-25 (similar to G9a and SUV39H), showed the loss of heterochromatin tethered to the nuclear lamina in C. *elegans*.[4] Multiple knockout of H3K9-methylating six KMTs resulted in the complete loss of electron-dense heterochromatin and the collapse of heterochromatin foci.[11] However, mechanisms by which H3K9 methylation-related modifiers work together to organize heterochromatin in the post-mitotic differentiated cells are not well known.

[1]Department of Life Science, Chung-Ang University, Seoul 06974, South Korea
[2]These authors contributed equally
[3]Lead contact
*Correspondence: jungkim@cau.ac.kr
https://doi.org/10.1016/j.isci.2024.110380

Histone lysine methyltransferases and demethylases (KDMs) regulate cell differentiation by balancing between writing and erasing methylation marks on cell type-specific gene elements.[12,13] The KDM3 family is a group of demethylases that are specific to mono- and di-methylation at H3K9 and involved in transcriptional activation.[14,15] The KDM3 family is crucial for cell survival and proliferation in highly dividing cells, such as prostate cancer, leukemia, and hepatocellular carcinoma cells.[15–17] However, the role of KDM3 in reorganizing heterochromatin regions to facilitate functional activation of tissue-specific genes and suppress lineage-inappropriate genes in terminally differentiated cells is not yet fully understood.

The functional physiology of differentiated cells is manifested through molecular interactions and complex networks encoded by genetic information. Multi-dimensional epigenomic networks shed light on gene regulatory networks (GRNs) in *in vivo* systems, resulting in the visualization of hidden biomolecular interactions. GRNs reveal cell type-specific development, differentiation, and cellular functions by controlling the transcriptional expression of signal molecules, transcription factors, and regulatory interactions.[18,19] Studying the network structure of integrated genomes and epigenomes contributes to a better understanding of spatial and temporal regulation of gene expression during differentiation and aging.[20] It is also possible to measure the network strength of gene regulation-epigenetic modification via the perpetual imbalance of homeostasis during aging.

Here, we aimed to understand the H3K9-mediated heterochromatin reorganization by constructing epigenomic networks integrated with physiological assays and multiple genome-wide analyses using a fully differentiated retina as an aging model system. We found that haploinsufficiency of *Kdm3b* is associated with fewer cone photoreceptors via increased lineage-inappropriate apoptotic genes and induced alterations of cone ribbon synapses due to the gain of heterochromatic features at functional cell type genes. Furthermore, KDM3B is required to maintain the integrated GRN strength that represents normal homeotic regulation by heterochromatin reorganization in the mouse retina during aging.

RESULTS

Characterization of heterochromatin organization factors involved in retinal aging

The retina is composed of six neuronal cell types including rod and cone photoreceptors (Figure 1A). To investigate the reorganization pattern of heterochromatin during retinal aging, we observed the distribution of heterochromatin in the nuclei of retinal cells with retinal cell type-specific markers and DAPI staining. Heterochromatin was detected at the nuclear periphery and within chromocenters in cone photoreceptors of 2-month-old mice. In contrast to this conventional pattern, the cone nuclei in 18-month-old mice showed less condensed heterochromatin with a decreased number and mean area of chromocenter, but the distribution of heterochromatin in rods and other retinal cells did not change in both 2- and 18-month-old mice (Figures 1B, 1C, S1A, and S1B). We also observed the distribution of silencing histone modifications (H3K9me1/2/3) as well as active modifications (H3K9ac and H3K4me3) in cone and rod cells during aging. H3K9me2/3 was abundant in the heterochromatin at the nuclear periphery in 2-month-old mice with conventional nuclear architecture, whereas H3K9me2/3 showed unusual distribution in both euchromatin and heterochromatin (but not in chromocenters) in 18-month-old mice (Figure S1C). However, we have not found significant differences in the distributions of H3K9me1, H3K9ac, and H3K4me3 between 2- and 18-month-old mice (Figure S1C). These data indicate that genome-wide organization of heterochromatin is altered in cones during aging.

To investigate whether epigenetic regulators are involved in the alteration of heterochromatin features during retinal aging, we next performed gene expression profiling by using RNA sequencing (RNA-seq) analysis from 1-, 6-, 12-, and 18-month-old mice retina. The strong agreement was shown for each biological replicate from the different time points (Figure S1D). Given the criteria of FPKM >20.0 and variance-mean ratio (or Fano factor) with each biological replicate under 1 and at least one group <0.5, 865 differentially expressed transcripts (DETs) were obtained by pairwise comparisons of samples (Figure 1D; Table S1). To cluster genes into groups based on their expression pattern during aging, we analyzed K-means clustering of DETs with $k = 6$. Six main clusters were plotted with expression patterns of transcripts involved (Figures 1E, 1F, and S1E). We focused on cluster 4, 5, and 6 that represent the gradually downregulated transcripts during aging. Transcripts in these clusters included ones known to be important in chromatin remodeling, such as *Kdm3b*, *Tet3*, *Ash1l*, *Ep300*, *Kdm2a*, *Cnnm4*, *Top1*, *Hdac2*, and *Dnmt3a* (Figures 1E and S1F; Table S1). Interestingly, *Kdm3b* is correlated with abnormalities of human eye including nystagmus, low vision, and learning of cerebellum-dependent optokinetic response.[21] We also confirmed that mRNA and protein levels of KDM3B were approximately 50% decreased in 18-month-old mice compared with 2-month-old mice (Figures 1G and 1H). Collectively, these results suggest that KDM3B may play a crucial role for the regulation of heterochromatin features in mice retina during aging.

Single-cell RNA-seq revealed a cell type-specific transcriptome during retinal aging

To identify the cell type-specific transcriptomes in individual cells during retinal aging, we performed single-cell RNA-seq (scRNA-seq) using the retinas of 1-, 12-, and 18-month-old mice. We retained a total of 10,933, 4,320, and 5,046 cells from 1-, 12-, and 18-month mouse retinas, respectively, which were taken forward for further analysis. Using the batch balanced kNN (BB *k* NN)[22] to correct for batch effects across different samples, we filtered our dataset to 20,299 single cells grouped into 18 clusters with 514 median genes and 1,144.5 median unique molecular identifiers per cell (Figures 2A and S2A; Table S2). Based on known cell type-specific markers, we identified rod photoreceptors (*Rho*, *Nrl*, *Gnat1*, *Pde6a*, and *Nr2e3*), cone photoreceptors (*Arr3*, *Gnat2*, *Ccdc136*, *Opn1mw*, and *Opn1sw*), bipolar cells (*Otx2*, *Ttr*, and *Grik1*), amacrine cells (*Nfix*, *Prox1*, and *Pcp4*), and microglia cells (*Tyrobp*, *C1qb*, and *C1qa*)[23–25] but no horizontal cells and ganglion cells that could not have tolerated the dissociation and capture protocols used (Figure 2A). Interestingly, our data revealed the presence of multiple transcriptionally distinct clusters within the rod photoreceptors (12 clusters). Moreover, two clusters (8 and 16) expressed markers from multiple retinal cell types (Figure 2A); thus, we re-classified individual cells, except for rod photoreceptors (12 clusters), into cell populations

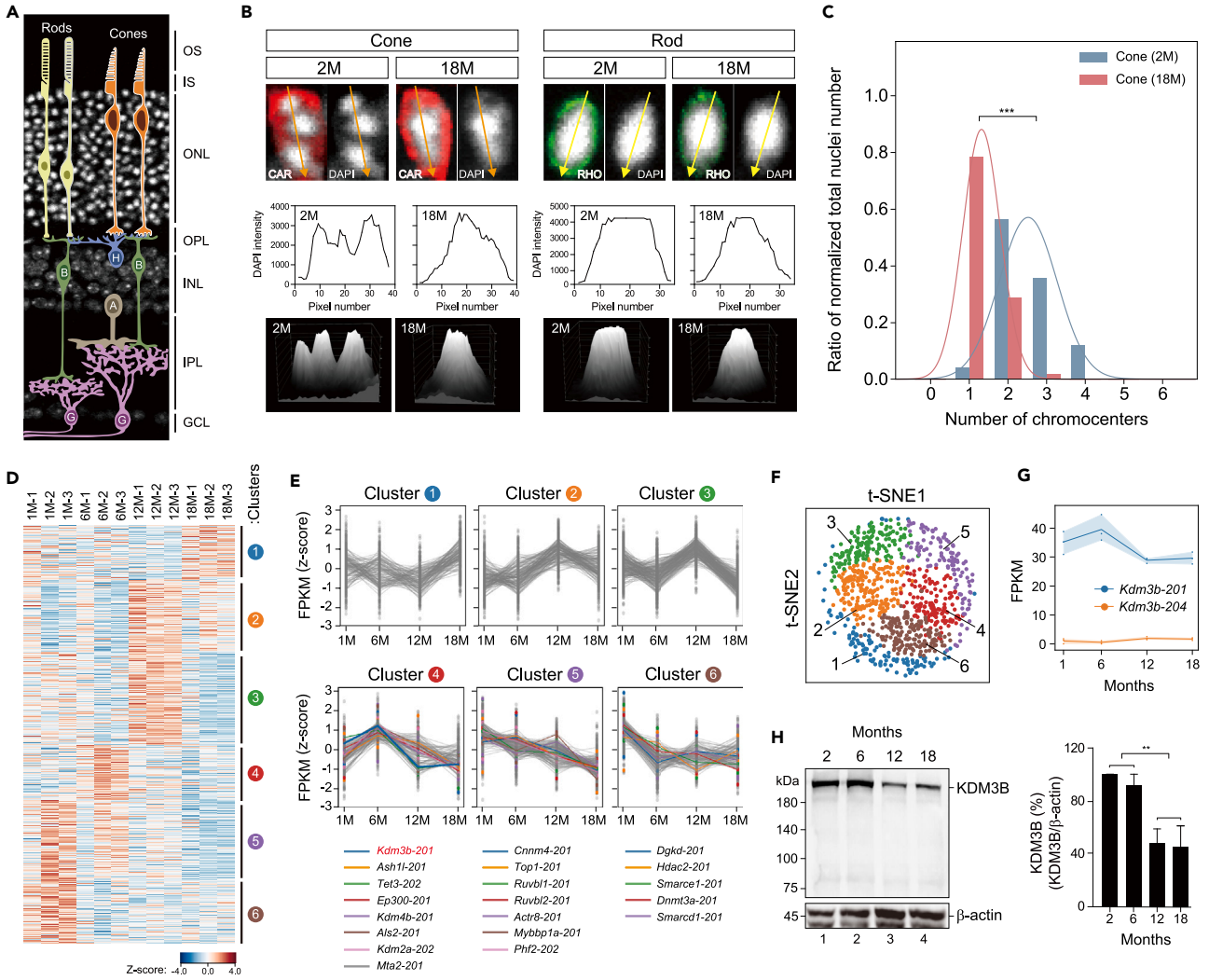

Figure 1. Characterization of heterochromatin organization and transcriptomic profiling during retinal aging

(A) Schematic representation of neural retina structure. A, amacrine; B, bipolar; G, ganglion; H, horizontal cells.

(B) Representative immunofluorescent confocal images of photoreceptor nuclei stained with cone arrestin (CAR) (red), RHO (green), and DAPI (white). Quantification of the intensity of DAPI in nuclei of cones or rods (lower).

(C) Quantification of the number of chromocenters in nuclei of cones. $N = 3$ eyes from C57bl6 mice, $n = 4$ images from each eye. ***$p < 0.001$ versus with data of 18 months by Mann-Whitney U test.

(D) Hierarchically clustered heatmap of transcripts with each biological replicates and at least one group <0.5 that were differentially expressed.

(E) Clustering analysis was developed by the *k*-means method (with $k = 6$) on the gene expression profiles.

(F) t-SNE plot revealing 6 distinct clusters identified from 1-, 6-, 12-, and 18-month-old mouse retinas.

(G) The expression level of *Kdm3b* transcripts (*Kdm3b*-201 and -204) in the mouse retinas.

(H) Whole retinal lysates of 2-, 6-, 12-, and 18-month-old mouse were immunoblotted using anti-KDM3B antibody (left). Signal intensity of KDM3B was quantified using ImageJ software (right). At least 25 mg of tissue was pooled for each sample (>8 retinas at 2, 6, 12, and 18 months). **$p < 0.01$ compared with 12- and 18-month mice by an independent two-sample t test.

See also Figure S1 and Table S1.

according to similarities in their transcriptome profiles. We finally obtained five clusters of retinal cell types (Figure 2B; Table S2); the gene expression of selected photoreceptor cell markers (rod: *Rho* and *Nrl*; cone: *Opn1mw* and *Opn1sw*) and genes involved in chromatin remodeling during aging was represented using t-distributed stochastic neighbor embedding (t-SNE) plots (Figure S2B). Gene expression analysis revealed that *Kdm3b*, *Ep300*, *Cnnm4*, *Dgkd*, *Kdm2a*, *Ash1l*, *Tet3*, and *Top1* were broadly expressed in all subclasses (Figure S2C).

To further investigate the transcriptomic dynamics in scRNA-seq, we measured the difference in mRNA abundance for individual genes through the estimation of mRNA stability in each retinal cell during aging.[26] mRNA stability (a derivative of spliced and unspliced mRNA abundance) is determined by the balance among transcription, splicing, and degradation processes[27] (Figure 2C). To measure mRNA stability, we

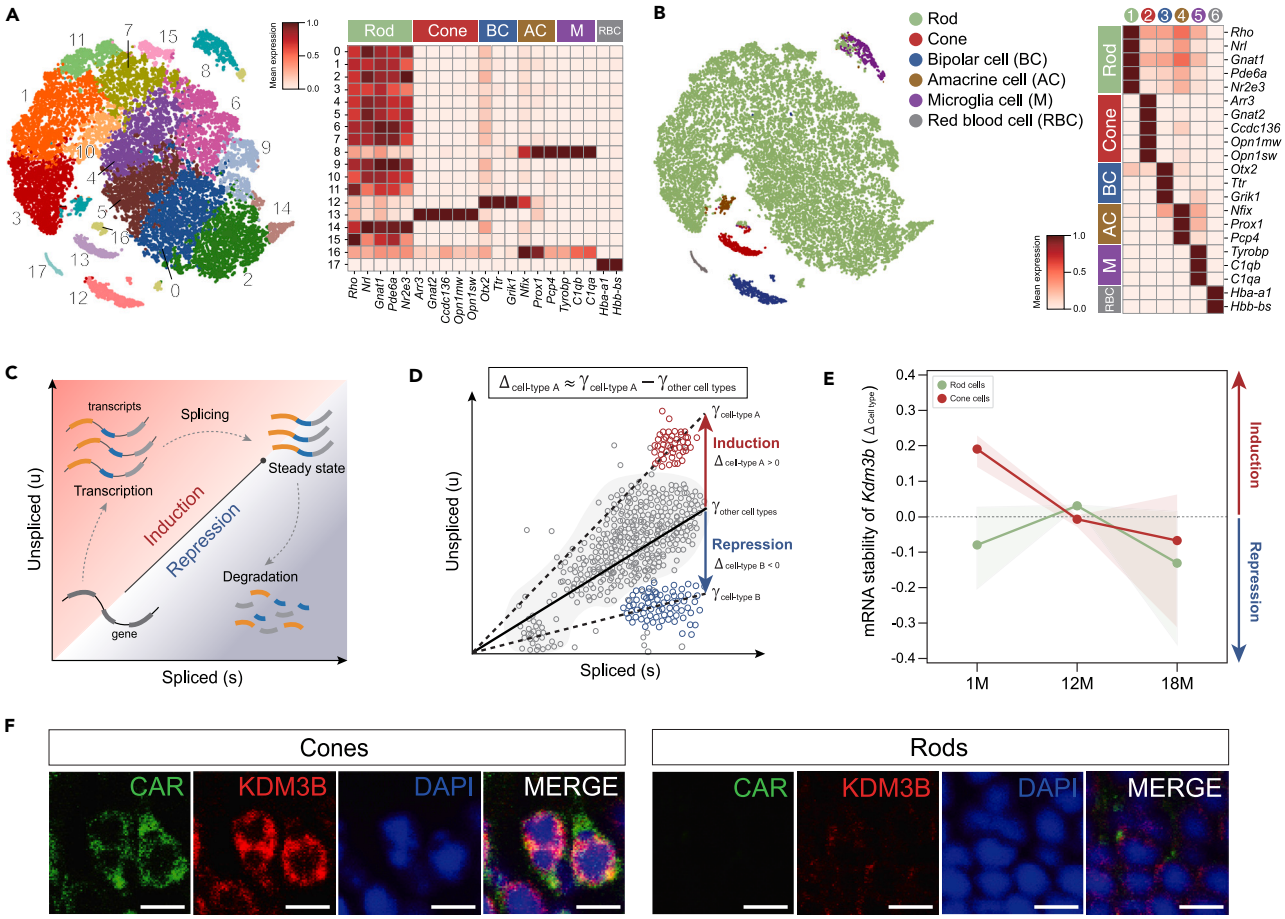

Figure 2. Single-cell transcriptome analysis and mRNA stability of *Kdm3b* during retinal aging

(A) t-SNE visualization of 1-, 12-, and 18-month mice retinas obtained from scRNA-seq analysis (left). Feature expression heatmap showing the retinal cell type-specific markers (18 groups) (right).

(B) t-SNE visualization of annotated 5 distinct major classed retinal populations (rod, cone, bipolar, amacrine, and microglia cell) with retinal cell type-specific markers in 1-, 12-, and 18-month mice (left). Feature expression heatmap showing the retinal cell type-specific markers (right).

(C) Model of transcriptional dynamics and phase portrait of mRNA stability.

(D) The mRNA stability ($\gamma_{\text{cell type A}}$) and relative mRNA stability ($\Delta_{\text{cell type A}}$) in specific cell population.

(E) The mRNA stability of *Kdm3b* in cones (red) or rods (green) compared to other cell types in 1-, 12-, and 18-month-old mice retinas.

(F) Immunostaining of KDM3B (red), CAR (green), and DAPI in 2-month mice retinas. Scale bar: 5 μm.

See also Figure S2 and Table S2.

estimated the equilibrium rate γ, which is the key factor underlying RNA velocity and gene abundance (Figure 2D). During the induction of gene expression, unspliced premature mRNA levels and the estimated slope γ are higher relative to those in the equilibrium state. In contrast, during repression of gene expression, spliced mature mRNAs are degraded, and γ is lower than the equilibrium rate. In addition, previous studies have shown that measurement of the divergence score for γ represents a reduction in transcriptional homeostasis during aging.[28] Therefore, we hypothesized that the mRNA stability of individual genes in a specific cell type ($\gamma_{\text{cell type}}$) increased ($\Delta > 0$) if relatively induced as compared to that in other cell types ($\gamma_{\text{other cell types}}$), while the mRNA stability of a specific gene decreased ($\Delta < 0$) if relatively reduced as compared to that in other cells ($\gamma_{\text{other cells types}}$). The difference (Δ) in γ of a particular cell type can be computed by measuring the difference between the observed production (Figure 2D). To test this hypothesis, we measured the difference (Δ) in mRNA stability of each cell type compared to other cells in 1-, 12-, and 18-month-old mice retinas (Figures 2E and S2D; Table S2). Interestingly, the mRNA stability of *Kdm3b* gradually decreased in cones, but the mRNA stability of *Kdm3b* fluctuated in rods from 1- to 18-month-old mice (Figures 2E and S2D). Furthermore, we observed the mRNA stability of chromatin remodelers in cone and rod cells. Most chromatin remodelers exhibited changes in mRNA stability regardless of aging in both cone and rod cells (Figure S2E). Using immunohistochemistry (IHC), we found that the KDM3B protein expression was highly enriched in cone cells, which suggested that it plays an important role in the maintenance of cellular functions in cone cells (Figures 2F and S2F). Taken together, these results suggest that the mRNA stability of *Kdm3b* in cone cells gradually decreases during aging and induces the deconstruction of functional homeostasis in cone cells.

Abnormal retinal phenotypes in *Kdm3b*$^{+/-}$ mice

To determine the cellular and molecular functions of KDM3B in the retina, we generated *Kdm3b* functional heterozygote mice (Figures S3A and S3B). We confirmed that the mRNA and protein levels of *Kdm3b* were approximately 50%–80% reduced in *Kdm3b*$^{+/-}$ retinas (Figures S3C and S3D). Additionally, public mRNA-seq data (GSE74660) from mice retina showed that *Kdm3b* continued to increase to post-natal 28 days (P28) in whole retina and cone cells[29] (Figure S3E). We clearly detected smaller eyes and abnormal corneal phenotypes in 12-month-old *Kdm3b*$^{+/-}$ mice compared with 1-month-old mice (Figure S3F). To further demonstrate the functional role of *Kdm3b* in the eye, we investigated the structural and morphological differences in the 1-, 6-, and 12-month-old *Kdm3b*$^{+/+}$ and *Kdm3b*$^{+/-}$ mice retina by measuring the thickness. The thickness of outer nuclear layer (ONL) was thinner in 12-month-old *Kdm3b*$^{+/-}$ than the *Kdm3b*$^{+/+}$ mice retinas but not in 1-month-old *Kdm3b*$^{+/+}$ and *Kdm3b*$^{+/-}$ mice retinas (Figure S3G). Consistently, the number of nuclei in the ONL was markedly reduced in *Kdm3b*$^{+/-}$ mice retinas among both 6- and 12-month-old mice (Figure S3H). It is possible that the decreased ONL thickness in the *Kdm3b*$^{+/-}$ retina was caused by a reduced number of photoreceptor cell nuclei, including those of rod and cone cells. To determine whether photoreceptors decreased in the ONL of the *Kdm3b*$^{+/-}$ retina, we performed IHC with cone cell-specific (anti-CAR; cone arrestin) and rod cell-specific (anti-RHO; rhodopsin) antibodies. We found that *Kdm3b* haploinsufficiency induces different morphologies and reduced the number of cones in 12-month-old mice but was not associated with differences in the rods (Figures S3I and S3J).

To determine the progression of cone cells loss in aged *Kdm3b*$^{+/-}$ retinas, we examined the density of cone cells and the morphological changes of cone outer segment by whole-mount immunohistochemistry (Figure S3K). The mean length of the inner segment of cones was significantly decreased, and the mean length of the basal side was increased in 12-month-old *Kdm3b*$^{+/-}$ mouse retinas (Figures S3L and S3M). Interestingly, we observed that the mean presynaptic area of cone cells (pedicle) was smaller in the 12-month-old *Kdm3b*$^{+/-}$ mouse retinas (Figure S3N). In addition, the cone nuclei in the retinas of 2-month-old *Kdm3b*$^{+/-}$ mice had less heterochromatin condensation, as shown by a smaller mean area of chromocenters. Conversely, the distribution of heterochromatin within rod nuclei in the retinas of 2-month-old *Kdm3b*$^{+/-}$ mice remained unchanged (Figure S3O). These results suggest that *Kdm3b* haploinsufficiency induced morphological changes and loss of cone cells in the aged mouse retina.

Profiling of transcriptomic dynamics in *Kdm3b*$^{+/-}$ mouse retinas

To investigate the role of *Kdm3b* in aging mouse retinas, we analyzed DETs in 12-month-old *Kdm3b*$^{+/+}$ and *Kdm3b*$^{+/-}$ retina by RNA-seq. The principal component analysis plot showed that *Kdm3b*$^{+/-}$ retinas accounted for the largest variance, and biological replicates showed great reproducibility (Figure S4A). The volcano plots represented the statistical significance of DETs with respective fold changes ($p < 0.05$, absolute $\log_2$ fold change > 1) compared with the control group (Figure S4B). Application of DESeq2 with conservative access to the RNA-seq data gained from the *Kdm3b*$^{+/-}$ retinal samples confirmed 4,125 DETs (Figure S4C; Table S1). Gene ontology (GO) was applied to reveal the biological connection among the up- and downregulated differentially expressed genes (DEGs) in *Kdm3b*$^{+/-}$ mouse retinas, respectively (Figure S4D; Table S1). Consistently, gene set enrichment analysis revealed that genes associated with cellular responses to neuron apoptotic process and DNA damage stimulus were upregulated, while repressed genes in *Kdm3b*$^{+/-}$ mouse retinas were involved in synapse assembly and vesicle-mediated transport (Figure S4E). Additionally, selected genes were up- or downregulated in *Kdm3b*$^{+/-}$ mouse retinas, and the expression patterns of chosen genes, as determined by quantitative reverse-transcription PCR (RT-qPCR), were consistent with the expression profiles by RNA-seq (Figures S4F–S4H). These results indicate that KDM3B has a crucial role for cell death and synaptic transmission in the mouse retina.

Since KDM3B haploinsufficiency induced the expression of gene sets for mRNA splicing, we also investigated alternative splicing events in RNA-seq data. Identified splice site variants were categorized as 4,465 events for skipped exon, 544 events for 5′-splice site, 921 events for 3′-splice site, 628 events for mutually exclusive exon, and 1,004 events for retained intron (RI) (Figure S4I). These events showed the distribution of protein-coding genes (Figure S4J). RI is exemplified by the glycolytic enzyme, aldolase A (*Aldoa*). The *Aldoa* transcript in *Kdm3b*$^{+/+}$ mice did not include any introns between exon 7 and exon 10; however, introns were not removed in the *Kdm3b*$^{+/-}$ mouse retinas, suggesting a novel effect of KDM3B in transcript maturation (Figure S4K). In addition, we also found the exon skipping events on the *Gulp1* transcript, where exon 8 had a low read count in *Kdm3b*$^{+/-}$ mouse retinas (Figure S4L).

Site-specific regulation of H3K9 methylation patterns by KDM3B in mouse retinas

Because KDM3B is required for the physiological and functional roles of cone cells, we performed chromatin immunoprecipitation sequencing (ChIP-seq) analysis to determine whether KDM3B was directly involved in the regulation of gene expressions associated with cone function via histone demethylase activity. Over 17.8 million reads were obtained for KDM3B ChIP-seq; these were aligned to the mouse reference genome (GRCm38.p13.101), and peak calling was performed (Table S3). The majority of KDM3B peaks were globally found within $\pm$3 kb away from the transcription start site (TSS) (Figure 3A). The distribution of KDM3B-binding peaks signified that the KDM3B was localized in intergenic (58%) and intron (39%) regions (Figure 3B). To further test the functional importance of KDM3B in gene expression regulation, we examined the GO analysis of the KDM3B-binding peaks. Interestingly, the KDM3B ChIP signals were highly enriched for genes involved in nervous system development, such as visual perception, vesicle-mediated transport, chromatin organization, and synaptic vesicle endocytosis (Figure 3C; Table S3).

Previous studies have determined that KDM3B has demethylase activity for H3K9me1 and H3K9me2 but not H3K9me3.[15,30] To determine whether KDM3B associated with H3K9me1, H3K9me2, and H3K9me3 marks the same target genes, we performed H3K9me1, H3K9me2, and

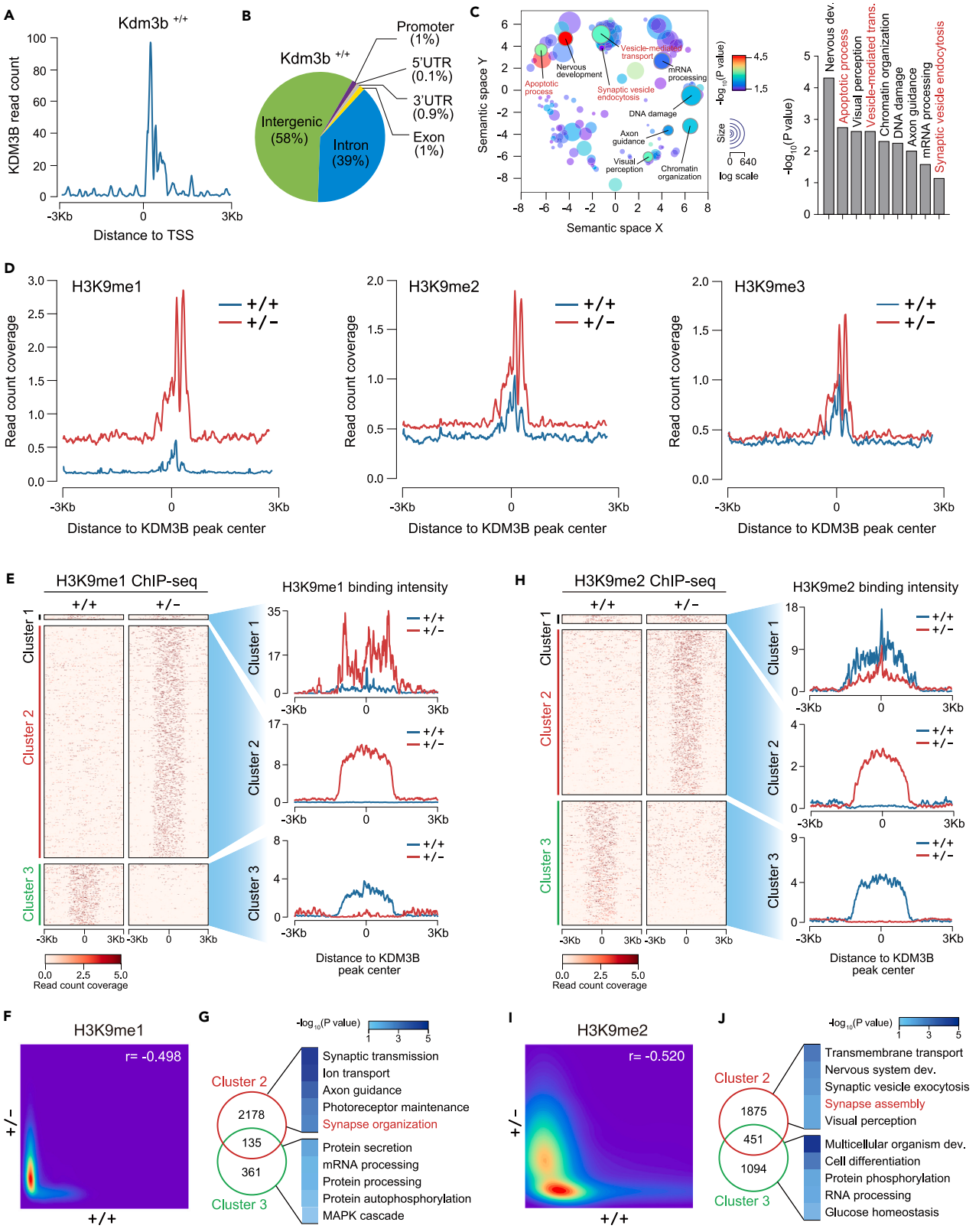
A
Kdm3b +/+
KDM3B read count
Distance to TSS
B
Kdm3b +/+
Promoter (1%)
5'UTR (0.1%)
3'UTR (0.9%)
Exon (1%)
Intron (39%)
Intergenic (58%)
C
Semantic space X
Semantic space Y
Nervous development
Vesicle-mediated transport
mRNA processing
Apoptotic process
Synaptic vesicle endocytosis
DNA damage
Axon guidance
Visual perception
Chromatin organization
-log10(P value)
Size
log scale
Nervous dev.
Apoptotic process
Visual perception
Vesicle-mediated trans.
Chromatin organization
DNA damage
Axon guidance
mRNA processing
Synaptic vesicle endocytosis
D
H3K9me1
H3K9me2
H3K9me3
+/+
+/-
Read count coverage
Distance to KDM3B peak center
E
H3K9me1 ChIP-seq
H3K9me1 binding intensity
Cluster 1
Cluster 2
Cluster 3
Read count coverage
Distance to KDM3B peak center
H
H3K9me2 ChIP-seq
H3K9me2 binding intensity
F
H3K9me1
r= -0.498
+/-
+/+
G
-log10(P value)
Cluster 2
2178
135
361
Cluster 3
Synaptic transmission
Ion transport
Axon guidance
Photoreceptor maintenance
Synapse organization
Protein secretion
mRNA processing
Protein processing
Protein autophosphorylation
MAPK cascade
I
H3K9me2
r= -0.520
J
Cluster 2
1875
451
1094
Cluster 3
Transmembrane transport
Nervous system dev.
Synaptic vesicle exocytosis
Synapse assembly
Visual perception
Multicellular organism dev.
Cell differentiation
Protein phosphorylation
RNA processing
Glucose homeostasis

Figure 3. The disruption of global H3K9 methylation in *Kdm3b*$^{+/-}$ mouse retinas

(A) Histogram shows the distribution of KDM3B peaks around transcriptional start sites (±3 kb).

(B) Pie chart of KDM3B enrichment distribution at promoters, exons, introns, 5′ UTRs, 3′ UTRs, and intergenic regions in *Kdm3b*$^{+/+}$ mouse retinas.

(C) Scatterplot of confidence scores for enriched gene ontologies associated with KDM3B ChIP-seq signal, clustered by functional similarity in the semantic space (left). Gene ontology of biological process is identified from KDM3B-enriched peaks (right).

(D) Plots of H3K9me1/2/3 ChIP-seq signal intensity relative to the center of KDM3B occupied sites (±3 kb) in *Kdm3b*$^{+/+}$ and *Kdm3b*$^{+/-}$ mouse retinas.

(E and H) Heatmap view of H3K9me1 (E) and H3K9me2 (H) ChIP-seq-read intensity around KDM3B peak center (±3 kb) detected in *Kdm3b*$^{+/+}$ and *Kdm3b*$^{+/-}$ mouse retinas. The plot shows the mean H3K9me1 and H3K9me2-binding intensities to the center of KDM3B peak, respectively.

(F and I) Scatter density plot of H3K9me1 (F) and H3K9me2 (I) read count coverage between *Kdm3b*$^{+/+}$ and *Kdm3b*$^{+/-}$ at KDM3B peak TSS regions.

(G and J) Gene ontology of biological process shows H3K9me1 (G) and H3K9me2 (J)-enriched peaks in *Kdm3b*$^{+/+}$ or *Kdm3b*$^{+/-}$ mouse retinas, respectively.

See also Figures S3–S5, Tables S1 and S3.

H3K9me3 ChIP-seq from 2-month-old *Kdm3b*$^{+/+}$ and *Kdm3b*$^{+/-}$ mouse retinas. Similar to KDM3B enrichment, the majority of H3K9me1, H3K9me2, and H3K9me3 peaks were globally found within ±100 kb away from the TSS, and most H3K9me1, H3K9me2, and H3K9me3 peaks were localized in intergenic and intron regions (Figures S5A and S5B; Table S3). Consistent with previous reports,[15,30] we also observed that KDM3B haploinsufficiency resulted in a dramatic increase in H3K9me1 and H3K9me2 levels, while the global patterns of H3K9me3 were not significantly different between *Kdm3b*$^{+/+}$ and *Kdm3b*$^{+/-}$ mice retinas (Figure 3D). To investigate the gene sets that are regulated by KDM3B-mediated H3K9 demethylation, we categorized H3K9me1/2 peaks at KDM3B-centered peaks into three clusters (Figures 3E and 3H): shared in both *Kdm3b*$^{+/-}$ and *Kdm3b*$^{+/+}$ mice retinas (cluster 1), only in *Kdm3b*$^{+/-}$ mice retinas (cluster 2), and only in *Kdm3b*$^{+/+}$ mice retinas (cluster 3). Centralization of ChIP-seq peaks indicated that the levels of H3K9me1/2 in cluster 2 increased only in *Kdm3b*$^{+/-}$ mice retinas; it is regulated in a KDM3B activity-dependent manner. Also, the enrichment of H3K9me1/2 in cluster 3 proceeded as a demethylase-independent function of KDM3B (Figures 3E and 3H). Consistently, the scatter density plot of the H3K9me1 and 2 level at KDM3B-centered peaks between *Kdm3b*$^{+/+}$ and *Kdm3b*$^{+/-}$ mice retinas revealed a markedly negative correlation (Figures 3F and 3I). Furthermore, we found that the H3K9me1/2-enriched target genes in *Kdm3b*$^{+/-}$ mice retinas (cluster 2) and the repressed genes are involved in synaptic transmission, synapse organization, and synapse assembly (Figures 3G and 3J). On the other hand, the H3K9me1/2 peaks in *Kdm3b*$^{+/+}$ (cluster 3) are enriched for the negative regulation of non-functional genes in retina (Figures 3G and 3J). Taken together, ChIP-seq analyses demonstrated that KDM3B is associated with H3K9me1 and H3K9me2 demethylation, suggesting that KDM3B exclusively regulates gene sets both neuronal homeostatic genes and cell death-related genes.

KDM3B upregulates the expression of synaptic genes through the erasure of H3K9me1 and H3K9me2 signatures

The balance between histone methylation and demethylation is highly correlated with transcriptional regulation.[12,31] We next determined the molecular mechanism by which KDM3B reduced the stimulation of synapse assembly genes in *Kdm3b*$^{+/-}$ mice via integration with ChIP-seq and RNA-seq analysis. Approximately 62.5% (1,240 genes) and 61.5% (1,028 genes) of upregulated or downregulated DEGs overlapped with all KDM3B ChIP-seq peaks (Figures 4A and 4B). Consistent with RNA-seq analysis, GO analysis showed that the genes which KDM3B bounded and upregulated simultaneously were involved in DNA damage stimuli and apoptotic process, while downregulated genes in *Kdm3b*$^{+/-}$ mice were exclusively enriched for neuronal development, synapse assembly, and vesicle-mediated transport (Figures 4C–4F; Table S3). We next focused on the 2,268 up- or downregulated DEGs in *Kdm3b*$^{+/-}$ mice to determine whether gene expression was modulated by the histone demethylation activity of KDM3B. The levels of H3K9me1 and H3K9me2 were significantly increased in association with downregulated genes in *Kdm3b*$^{+/-}$ mice, revealing the deposition of histone methylation due to the ablation of KDM3B enzymatic functions (Figure 4G). KDM3B was enriched on the synapse assembly genes, including *Nrxn2* and *Erc2*, which were downregulated in *Kdm3b*$^{+/-}$ mice (Figure 4H). Based on ChIP-seq data, we selected ten target genes, such as synapse assembly genes and apoptotic genes, that were validated by ChIP-qPCR. KDM3B was enriched on the target gene promoters (within −2 kb from TSS) representing the normal range of ChIP-seq peaks for H3K9me1 and H3K9me2 in *Kdm3b*$^{+/+}$, and that signal was significantly elevated in *Kdm3b*$^{+/-}$ mouse retinas (Figures 4I and S5C). We additionally validated the expression profile of the target gene, the recruitment kinetics of KDM3B, and the status of H3K9 methylation using RT-qPCR and ChIP-qPCR analyses during the aging process. Importantly, our findings closely paralleled those observed in *Kdm3b*$^{+/-}$ mouse retinas (Figure S5D). These results suggest that histone demethylase activity of KDM3B modulated the transcriptional dynamics of synaptic and apoptotic genes by balancing of the H3K9 methylation status.

Cell type-specific transcriptomic dynamics in *Kdm3b*$^{+/-}$ mouse retinas

To confirm the cone photoreceptor-specific regulation of *Kdm3b*, we further tested whether transcriptional alterations in *Kdm3b*$^{+/-}$ mice occur in cone cells using scRNA-seq analysis. Following multiple quality control and filtering steps, 17,787 cells from *Kdm3b*$^{+/-}$ 12-month-old mice retina were analyzed, and their transcriptomes were compared to the corresponding wild type. At least 18 distinct cell populations (cell clusters) were observed in *Kdm3b*$^{+/+}$ and *Kdm3b*$^{+/-}$ mouse retinas (Figures 5A, 5B, S6A, and S6B; Table S2). Using characteristic retinal cell markers, five retinal cell types were detected and classified as rod, cone, bipolar, amacrine, and microglia cells (Figure 5C).

Using GO enrichment analysis of the gene sets representing each cell clusters, we found that the upregulated DEGs in *Kdm3b*$^{+/-}$ cone cells were gene sets enriched for mRNA splicing and apoptotic processes, and the downregulated DEGs were associated with nervous system development and the maintenance of presynaptic active zone structure; both exhibited a similarly uniform pattern of expression in bulk retinal tissue RNA-seq analysis (Figure 5D; Table S2). Furthermore, we studied the mRNA stability of KDM3B target genes in cones and rods.

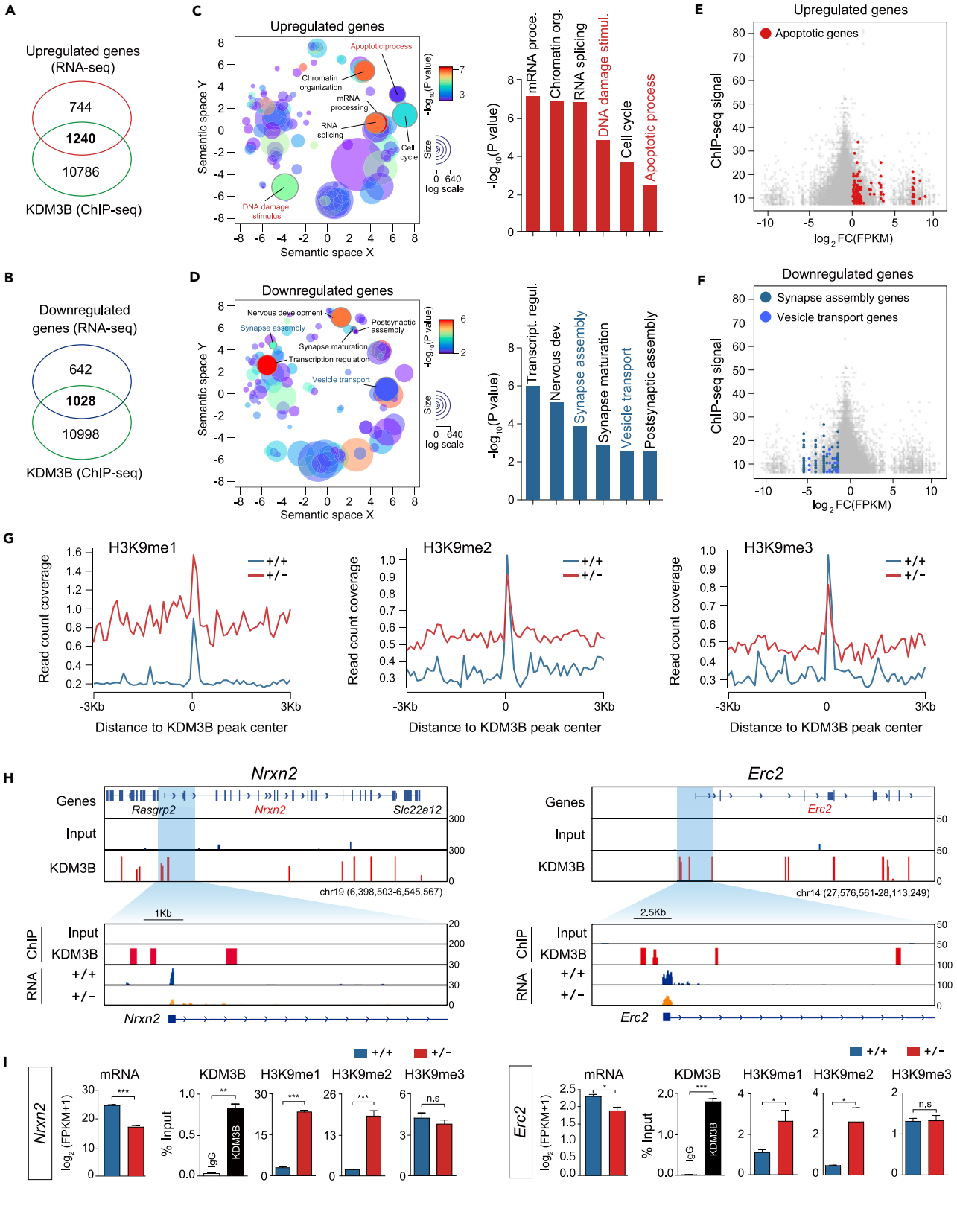
A
Upregulated genes (RNA-seq)
744
1240
10786
KDM3B (ChIP-seq)
B
Downregulated genes (RNA-seq)
642
1028
10998
KDM3B (ChIP-seq)
C
Upregulated genes
Apoptotic process
Chromatin organization
mRNA processing
RNA splicing
Cell cycle
DNA damage stimulus
Semantic space X
Semantic space Y
-log10(P value)
Size
0 640
log scale
-log10(P value)
mRNA proce.
Chromatin org.
RNA splicing
DNA damage stimul.
Cell cycle
Apoptotic process
D
Downregulated genes
Nervous development
Synapse assembly
Postsynaptic assembly
Synapse maturation
Transcription regulation
Vesicle transport
Semantic space X
Semantic space Y
-log10(P value)
Size
0 640
log scale
-log10(P value)
Transcript. regul.
Nervous dev.
Synapse assembly
Synapse maturation
Vesicle transport
Postsynaptic assembly
E
Upregulated genes
Apoptotic genes
ChIP-seq signal
log2 FC(FPKM)
F
Downregulated genes
Synapse assembly genes
Vesicle transport genes
ChIP-seq signal
log2 FC(FPKM)
G
H3K9me1
H3K9me2
H3K9me3
+/+
+/-
Read count coverage
-3Kb
0
3Kb
Distance to KDM3B peak center
H
Nrxn2
Genes
Rasgrp2
Nrxn2
Slc22a12
Input
KDM3B
chr19 (6,398,503-6,545,567)
1Kb
ChIP
RNA
Input
KDM3B
+/+
+/-
Nrxn2
Erc2
Genes
Erc2
Input
KDM3B
chr14 (27,576,561-28,113,249)
2.5Kb
ChIP
RNA
Input
KDM3B
+/+
+/-
Erc2
I
+/+
+/-
Nrxn2
log2 (FPKM+1)
mRNA
% Input
KDM3B
H3K9me1
H3K9me2
H3K9me3
IgG
KDM3B
n.s
Erc2
log2 (FPKM+1)
mRNA
% Input
KDM3B
H3K9me1
H3K9me2
H3K9me3
IgG
KDM3B
n.s

Figure 4. The global correlation between transcriptome and heterochromatic dynamics during mouse retinal aging

(A and B) Venn diagram showing the overlap between the genes including KDM3B peaks and upregulated (A) or downregulated (B) KDM3B target genes based on RNA-seq data.

(C and D) Scatterplot of confidence scores for enriched gene ontologies associated with upregulated (C) and downregulated genes (D), and their enrichments for KDM3B. Gene ontology shows up- and downregulated genes obtained from integration with RNA-seq and ChIP-seq data.

(E and F) Scatterplot showing changes in the expression of apoptotic genes in upregulated (E) or synapse-assembly and vesicle transport genes in downregulated genes (F) in *Kdm3b*$^{+/+}$ and *Kdm3b*$^{+/-}$ mouse retinas and their enrichments for KDM3B.

(G) Plots of H3K9me1/2/3 ChIP-seq signal intensity relative to the center of KDM3B occupied sites (±3 fb) in *Kdm3b*$^{+/+}$ and *Kdm3b*$^{+/-}$ mouse retinas.

(H) ChIP-seq tracks of KDM3B in *Kdm3b*$^{+/+}$ along the *Nrxn2* and *Erc2* locus. Selected genomic elements (shaded with light cyan) indicate KDM3B ChIP-seq peaks at *Nrxn2* and *Erc2* promoter regions.

(I) Recruitment and the presence of KDM3B, H3K9me1/2/3 at *Nrxn2* and *Erc2* promoter regions are validated by ChIP-qPCR. **p* value <0.05, ***p* value < 0.01, ****p* value < 0.001 compared with *Kdm3b*$^{+/-}$ by an independent two-sample t test. Data are represented as the mean ± SEM.

See also Figure S5 and Table S3.

Interestingly, the apoptotic genes (*Parp1* and *Pdcd4*) were upregulated, and synaptic-related genes (*Pclo* and *Erc2)* were downregulated in the cone cells of *Kdm3b*$^{+/-}$ mice, while inflammatory response and protein ubiquitination were enriched in rod cells of *Kdm3b*$^{+/-}$ mice (Figures 5E, 5F, and S6C; Table S2). These results indicated that transcriptome dynamics upon ablation of KDM3B selectively regulated the expression of gene sets involved in neuronal apoptosis and synaptic transmission, particularly in cone cells.

Induction of apoptotic signals and synaptic dysfunction in cone photoreceptors of *Kdm3b*$^{+/-}$ mouse retinas

Previous studies suggested that apoptosis occurs in pathologic photoreceptor cell death in several mouse models of retinal degeneration.[32,33] Since the number of cone cells was reduced in *Kdm3b*$^{+/-}$ aged mice, we investigated whether retinal cells in the ONL were damaged due to the death of photoreceptors. We first detected the presence of Müller glial cells, which were involved in the clearance of damaged cells and retinal regeneration, using anti-GFAP antibodies.[34] The mean Müller cell counts were significantly increased in 6- and 12-month-old *Kdm3b*$^{+/-}$ retinas compared with age-matched *Kdm3b*$^{+/+}$ retinas (Figure S7A). To further confirm whether retinal cell damage induces photoreceptor cell death through apoptosis, we stained 1- and 12-month-old *Kdm3b*$^{+/+}$ and *Kdm3b*$^{+/-}$ retinas with the executive apoptotic marker, cytochrome *c*. The intensity of cytochrome *c* was significantly increased in 12-month-old *Kdm3b*$^{+/-}$ retinas relative to 1-month-old *Kdm3b*$^{+/-}$ retinas; this difference was not present in *Kdm3b*$^{+/+}$ retinas (Figure S7B). Interestingly, we observed an increased release of cytochrome *c* in the cone cells of 12-month-old *Kdm3b*$^{+/-}$ retinas (Figures 6A and S7C). Furthermore, we used TUNEL staining to determine whether degenerating cone cells underwent genomic DNA fragmentation through apoptosis. TUNEL-positive apoptotic cone cells also markedly increased in 12-month-old *Kdm3b*$^{+/-}$ retinas (Figures 6B, S7D, and S7F). It is suggested that loss of *Kdm3b* in aging induces apoptosis of cone cells, and finally, this phenomenon causes cone cell death in the retina.

Photoreceptor ribbon synapses are specialized synaptic structures in the outer plexiform layer where visual signals are transmitted from photoreceptors to bipolar and horizontal cells.[35] Since functional KDM3B is required for the expression of synaptic and vesicle transport gene sets, we examined whether haploinsufficiency of *Kdm3b* affected changes in the functional morphology of cone ribbon synapses. In the result, the mean area of cone synaptic terminals and the number of ribbon synapses were significantly reduced in 12-month-old *Kdm3b*$^{+/-}$ retinas (Figure 6C, Video S1). To observe the further details of cone synaptic terminal structure, we performed transmission electron microscopy (TEM). *Kdm3b* deficiency did not affect the length of ribbon synapses and the number and distance from ribbon synapse to vesicles in the presynaptic regions of both rods and cones (Figure S7E). However, the mean number of docked vesicles of cone ribbon synapses was decreased in 12-month-old *Kdm3b*$^{+/-}$ retinas (Figure 6D). To further investigate the physiological role of KDM3B *in vivo*, we analyzed electroretinograms in 6-month-old *Kdm3b*$^{+/+}$ and *Kdm3b*$^{+/-}$ mice under light-adapted (photopic) and dark-adapted (scotopic) conditions (Figures S8A and S8B). Under photopic conditions, the a-wave amplitude was not significantly different, but b-waves were significantly reduced in 6-month-old *Kdm3b*$^{+/-}$ mice (Figure S8A). In contrast, the amplitude of a- and b-waves in scotopic conditions and rod-mediated outer retinal activity were not different between *Kdm3b*$^{+/+}$ and *Kdm3b*$^{+/-}$ mice (Figure S8B). These results suggest that synapse transmission from cone cells to cone bipolar cells was impaired in 6-month-old *Kdm3b*$^{+/-}$ mice.

KDM3B directly regulates neuronal apoptotic and synaptic functions in cone photoreceptors

To further validate the observed phenotypes of cones were explicitly due to the cone cell-autonomous function of *Kdm3b*, we injected the *Kdm3b*-T2A-GFP AAV2.7m8 to *Kdm3b*$^{+/-}$ mice retina or *shKdm3b*-GFP AAV2.7m8 in the 8-month-old wild-type mouse retina by using subretinal injection method. Overexpression and knockdown constructs were designed to target the *Kdm3b* Jumonji C domain, which has demethylase enzymatic activity (Figure 6E, right). For the sufficient induction of the Adeno-associated virus (AAV) construct expression, we performed physiological assays after 2 weeks after injecting individual constructs (Figure 6E, left). We observed KDM3B signal in both shScramble-GFP-injected and uninjected cells, whereas KDM3B was not detected in *Kdm3b* knockdown cell by *shKdm3b*-GFP AAV2.7m8-infected 8-month mice retina (Figure S9A). Having determined the roles of the chromatin remodeling gene, *Kdm3b*, for the impairment of cone in aging through the reorganization of heterochromatin features (Figure 1), we first analyzed the reorganization pattern of heterochromatin in *shKdm3b*-GFP AAV2.7m8-infected 8-month-old mice retina. The mean area of the chromocenter was decreased in *shKdm3b*-GFP AAV2.7m8-injected cone cells, but the distribution of heterochromatin in rod cells did not change (Figure S9B, left). To examine the restorability of functional defects in *Kdm3b*$^{+/-}$ mice, we observed the heterochromatin pattern in p*CMV-Kdm3b*-T2A-GFP AAV2.7m8=infected

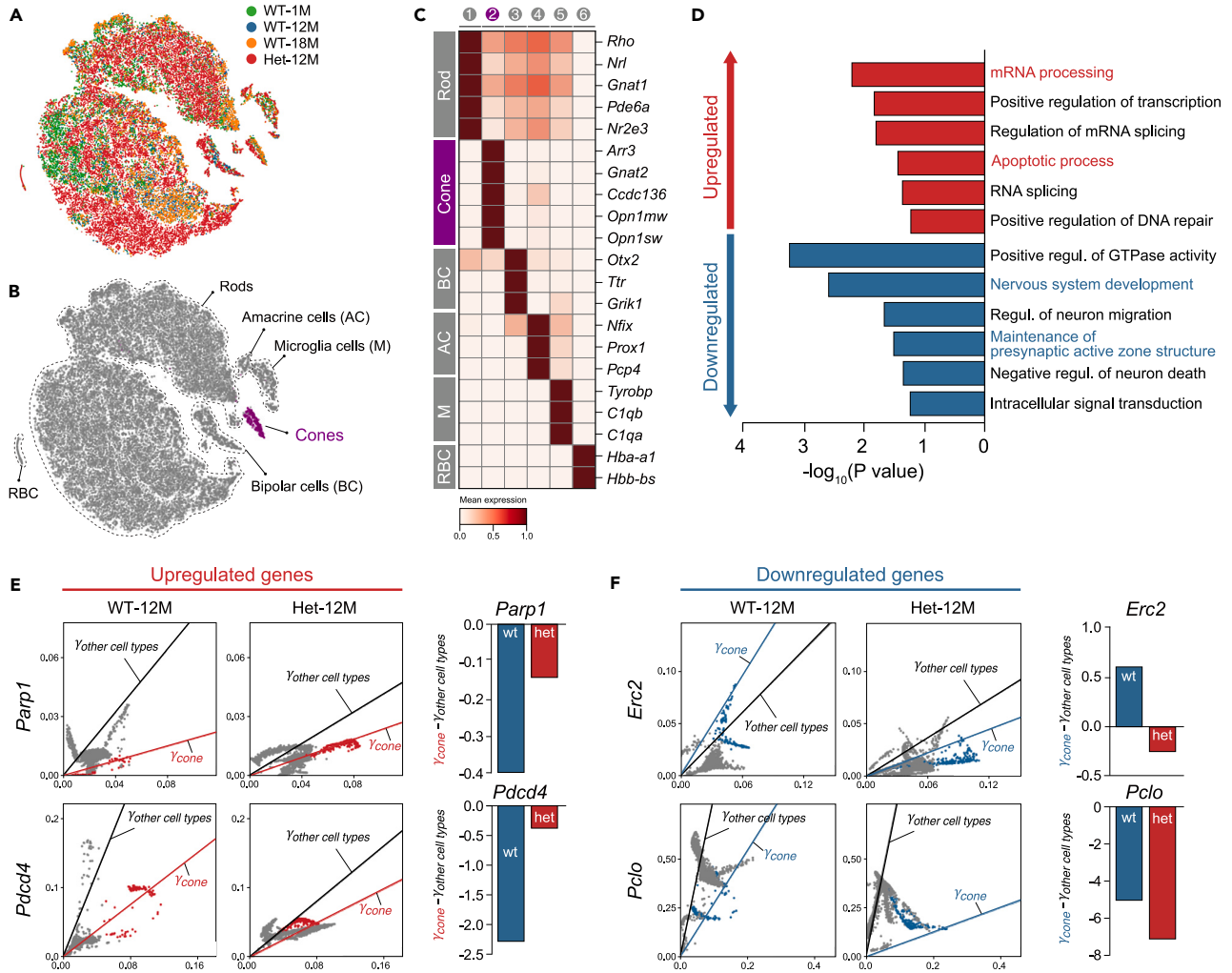

Figure 5. Alteration of single-cell transcriptome dynamics in *Kdm3b*$^{+/-}$ mouse retinas

(A) t-SNE visualization of 1-, 12-, and 18-month *Kdm3b*$^{+/+}$ and 12-month *Kdm3b*$^{+/-}$ retinal cells obtained from scRNA-seq analysis.

(B) Annotation of 5 distinct clusters in 1-, 12-, and 18-month *Kdm3b*$^{+/+}$ and 12-month *Kdm3b*$^{+/-}$ retina.

(C) Feature expression heatmap showing major retinal class markers across 5 retinal cell clusters.

(D) GO terms analysis in cone population.

(E and F) The mRNA stability of apoptosis-induced genes (*Parp1* and *Pdcd4*) (E) and synapse-related genes (*Erc2* and *Pclo*) (F) in cones of 12-month-old *Kdm3b*$^{+/+}$ and *Kdm3b*$^{+/-}$ mouse.

See also Figure S6 and Table S2.

8-month-old *Kdm3b*$^{+/-}$ mouse retina. Similar to *Kdm3b*$^{+/+}$ mice, the cone nuclei in p*CMV-Kdm3b*-T2A-GFP AAV2.7m8-infected *Kdm3b*$^{+/-}$ mice showed more condensed heterochromatin with the increased mean area of chromocenter (Figure S9B, right). Next, we found that the released intensity of cytochrome *c* from mitochondria was significantly increased in *shKdm3b*-GFP AAV2.7m8-injected cone cells (CAR stained) compared with shScramble-GFP AAV2.7m8-injected wild-type controls (Figures 6F and S9C), whereas the released intensity of cytochrome *c* in cones from p*CMV-Kdm3b*-T2A-GFP AAV2.7m8-infected *Kdm3b*$^{+/-}$ mice was reduced compared with p*CMV*-GFP AAV2.7m8-infected *Kdm3b*$^{+/-}$ mice (Figures 6G and S9D). The results showed that Kdm3b haploinsufficiency changed the heterochromatin feature, which led to more apoptotic signals in cone cells.

Furthermore, the number of ribbon synapses in cone pedicles was significantly decreased in sh*Kdm3b*-GFP AAV2.7m8-infected *Kdm3b*$^{+/+}$ mice retinas compared with shScramble-GFP AAV2.7m8-infected *Kdm3b*$^{+/+}$ retinas (Figures 6H and S9E). On the other hand, *Kdm3b*$^{+/-}$ mice transduced with *Kdm3b*-T2A-GFP AAV2.7m8 showed that the number of cone ribbon synapses was significantly increased compared with control p*CMV*-GFP AAV2.7m8-infected *Kdm3b*$^{+/-}$ mice retinas (Figures 6I and S9F). Finally, we analyzed the mRNA expression level and the status of H3K9me at KDM3B target genes by RT-qPCR and ChIP-qPCR in sh*Kdm3b*-GFP AAV2.7m8-infected *Kdm3b*$^{+/+}$ mice retinas. The expression of the target genes was consistent with bulk retinal tissue RNA-seq, and H3K9me1 and H3K9me2 were significantly elevated

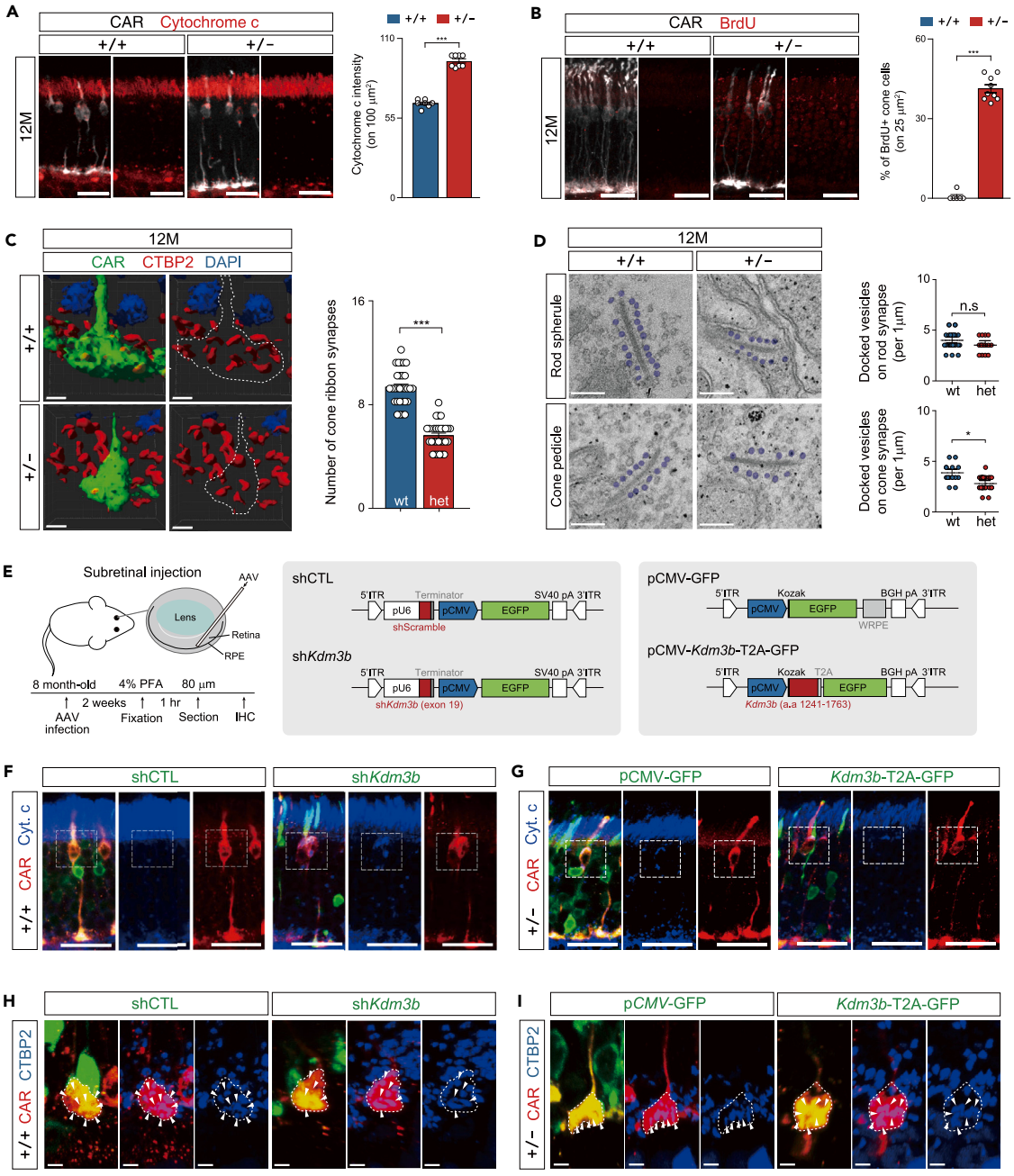

Figure 6. Induction of apoptosis and synaptic impairment of cones in *Kdm3b*$^{+/-}$ mice

(A) Double immunostaining with cytochrome *c* (red) and CAR (white) in 12-month-old *Kdm3b*$^{+/+}$ and *Kdm3b*$^{+/-}$ retinas (left). Scale bar: 20 μm. The signal intensity in the cell body of cytochrome *c*-positive cones in 100 μm^2 was measured (right).

(B) Apoptotic cells were detected by TUNEL assay (BrdU+ cells) in 12-month *Kdm3b*$^{+/+}$ and *Kdm3b*$^{+/-}$ retinas. BrdU (red) staining in cones (white) (left) and the percentage of BrdU-positive cones is quantified (right). Scale bar: 20 μm.

(C) 3D reconstruction images showing ribbon synapses in cones of 12-month-old *Kdm3b*$^{+/+}$ and *Kdm3b*$^{+/-}$ mice. Immunostaining with CTBP2 (red) and CAR (green) antibodies examined (left). The number of ribbon synapses is measured in a cone pedicle (right). Scale bar: 2 μm.

(D) TEM images of docked vesicles (shaded with light cyan) on the rod and cone ribbon synapses (left). Scale bar: 0.2 μm. The number of docked vesicles on the rod and cone ribbon synapse is quantified in 12-month-old *Kdm3b*$^{+/+}$ and *Kdm3b*$^{+/-}$ mice (0.1 μm of each ribbon synapse) (right).

Figure 6. *Continued*

(E) Outline of experimental design and Adeno-associated virus (AAV) reporter cassettes for knockdown and ectopic expression of KDM3B. $N = 2$ or 3 eyes from different mice, $n = 5$ images from each eye All data expressed as mean ± SD (A–E). ***p value <0.001 by independent two-sample t test. All data expressed as mean ± SEM.

(F and G) Immunostaining with cytochrome c (blue) and CAR (red) antibodies in 8-month-old *Kdm3b*$^{+/+}$ retinas following subretinal injection of shScramble-GFP or sh*Kdm3b*-GFP AAV2.7m8 (F), and *Kdm3b*$^{+/-}$ retinas after subretinal injection of p*CMV*-GFP or p*CMV-Kdm3b*-T2A-GFP AAV2.7m8 (G).

(H and I) Immunostaining with CTBP2 (blue) and CAR (red) antibodies in 8-month-old *Kdm3b*$^{+/+}$ retinas following subretinal injection of shScramble-GFP or sh*Kdm3b*-GFP AAV2.7m8 (H), and *Kdm3b*$^{+/-}$ retinas after subretinal injection of p*CMV*-GFP or p*CMV-Kdm3b*-T2A-GFP AAV2.7m8 (I).

See also Figures S1 and S7–S9 and Video S1.

in sh*Kdm3b*-GFP AAV2.7m8-infected *Kdm3b*$^{+/+}$ mice retinas (Figure S10). Taken together, these findings show that KDM3B is required for cone synaptic components that are associated with visual acuity during aging.

KDM3B associates with AP-1 transcription factors

Since KDM3B does not directly bind to DNA, KDM3B might be associated with DNA through binding to specific transcription factors. In leukemogenesis, KDM3B interacted with CBP, forming an activator complex during lmo2 transcription activation.[15] To identify potential new partners of KDM3B, we analyzed *de novo* motif discovery using the MEME-ChIP algorithm. We identified a list of 10 enriched motifs (Table S3). The two highly enriched *de novo* motifs show significant similarity to a known ZNF384 and transcription factors of AP-1 family, JUNB and FOS (JASPAR database), respectively (Figure S11A). Furthermore, we analyzed the positional distribution of ZNF384 and JUNB-enriched motifs using the Centrimo algorithm. Both ZNF384 and JUNB motifs are colocalized with KDM3B-ChIP peaks (Figure 7A). *De novo* motif analysis of the KDM3B ChIP-seq regions represented the potential binding regions for transcription factors that might co-occupy KDM3B-regulated genomic sites and potentially modulated its target genes. We confirmed whether AP-1 transcription factors are involved in KDM3B recruitment *in vivo*. Coimmunoprecipitation experiments showed that KDM3B was associated with c-Fos and JUNB in mice retina (Figures 7B and S11B). Additionally, ChIP-qPCR with c-Fos and JUNB antibodies confirmed that both transcription factors were associated in KDM3B target genes (Figures 7C and S11C). Taken together, these results suggest that KDM3B, c-Fos, and JUNB can physically interact and could regulate a set of KDM3B target genes.

Kdm3b haploinsufficiency accelerated the destruction of epigenomic network robustness

The diversity of neuronal structure and function is established by GRNs, which is produced by controlled changes in gene expression pattern and coordinated assemblages of specific regulatory linkages among specific genes.[18,20] To define the relationship of KDM3B with other transcriptional regulators and downstream cognate effectors between *Kdm3b*$^{+/+}$ and *Kdm3b*$^{+/-}$, we constructed KDM3B-centered epigenomic networks using integrated RNA-seq and KDM3B ChIP-seq analysis. The *Kdm3b*$^{+/+}$ network consisted of 1,697 genes with 3,498 links, and the *Kdm3b*$^{+/-}$ network consisted of 1,609 genes with 3,217 links (Figures S11D). The clustering coefficient (*Kdm3b*$^{+/+}$ = 0.318 versus *Kdm3b*$^{+/-}$ = 0.324) and the diameter of nodes were similar between the *Kdm3b*$^{+/+}$ and *Kdm3b*$^{+/-}$ networks, indicating a lack of a significant difference between the global properties of the networks. To further measure the structural difference strictly, the network dissimilarity concept ($D(G, G')$)[36,37] was introduced to the expanded network between *Kdm3b*$^{+/+}$ and *Kdm3b*$^{+/-}$ during aging. In the result, the D-value between the 12-month-old *Kdm3b*$^{+/+}$ and *Kdm3b*$^{+/-}$ showed relatively high dissimilarity (0.0018) than *Kdm3b*$^{+/+}$, which undergoes aging (0.0013), and between the 18-month-old *Kdm3b*$^{+/+}$ and 12-month-old *Kdm3b*$^{+/-}$ has low dissimilarity (0.0006) than the 12-month-old *Kdm3b*$^{+/+}$ and 12-month-old *Kdm3b*$^{+/-}$ (0.0018) (Figure 7D). These results showed that the haploinsufficiency of *Kdm3b* induced the alteration of structural relation in the entire gene network as well as diverse biological features.

Network robustness is a central question in systems biology and medicine, helping us understand why subtle changes or failures lead to disease.[38] From this point of view, we measured the network robustness between the *Kdm3b*$^{+/+}$ and *Kdm3b*$^{+/-}$ by random link removal. We simulated random link removal with a fraction f and measured the fraction of largest cluster size ($P(f)/P(0)$) as an order parameter (Figure 7E). Since all epigenomic networks of KDM3B are based on centralized KDM3B networks and finite-sized networks, we can predict that the critical threshold f_c goes to 1.[39] Therefore, we focused on the difference of $P(f)/P(0)$ for various f. The order parameters of all four *Kdm3b*$^{+/+}$ network stages obviously showed more robustness for link failure than the *Kdm3b*$^{+/-}$ network, but the order parameter of the random selected-genes network was no significant change (Figures 7E and S11E). These results imply that the *Kdm3b* haploinsufficiency causes epigenomic network dissimilarity, resulting in the acceleration of the network robustness destruction.

DISCUSSION

We demonstrated a critical function of H3K9-methylated heterochromatin coordinated by KDM3B in the selective modulation of the gene expressions, such as loss of heterochromatin at apoptotic genes and gain of heterochromatin at neuro-functional genes. KDM3B is a putative regulator of apoptotic signaling and synaptic transmission, playing a role as "balancer" of the retinal aging process especially in the cone photoreceptors. We generated heterozygote *Kdm3b* mice and focused on the function of KDM3B in the mouse retina via physiological, genetic, and multi-dimensional epigenomic analysis. We found that *Kdm3b* mRNA expression is similar between rods and cones during development, but the protein level is highly enriched only in differentiated cones. scRNA-seq of aging retinal cells revealed that KDM3B specifically downregulated its transcriptional activity in the cone cells but not in the rods (Figure 2). These imply that KDM3B has cell type specificity and different functional roles at the post-transcriptional and protein level.

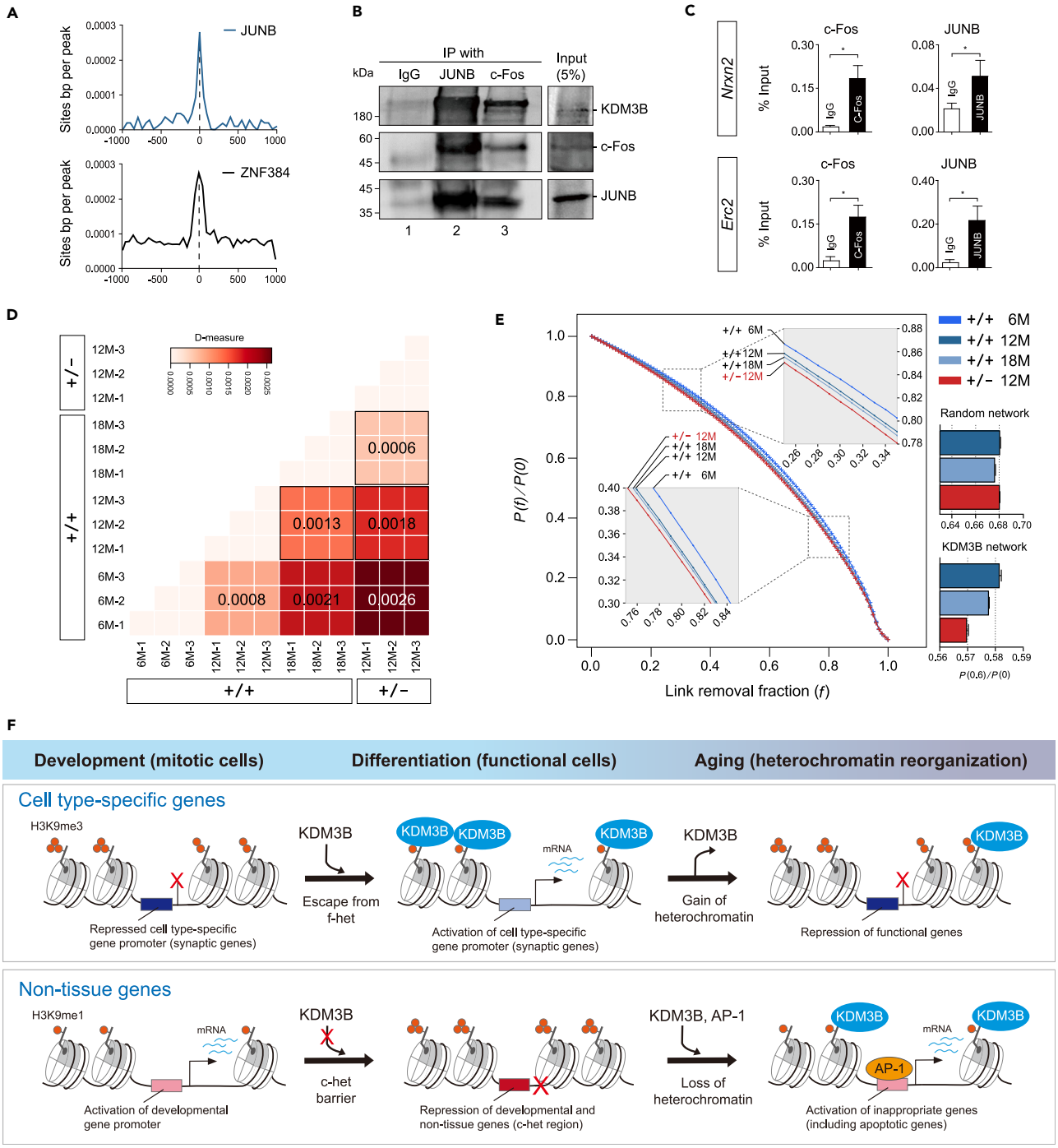

Figure 7. The measurement of structural difference and robustness of KDM3B-centered networks

(A) The graph represents the distribution of occurrence probabilities of the consensus sequences enriched under KDM3B ChIP-seq peaks relative to ZNF384 and JUNB motifs.

(B) Immunoblot showing co-immunoprecipitation of endogenous c-Fos and JUNB with KDM3B in mice retinas.

(C) Recruitment and presence of c-Fos and JUNB at *Nrxn2* and *Erc2* promoters are validated by ChIP-qPCR. **p* value <0.05 compared with IgG by an independent two-sample t test. Data are represented as the mean ± SEM.

(D) The matrix of dissimilarity *D*'s measured from each pair of networks in 6-, 12-, and 18-month *Kdm3b*$^{+/+}$ and 18-month *Kdm3b*$^{+/-}$ mouse retinas.

Figure 7. *Continued*

(E) The plot of nodes fraction that belong to the largest component in the KDM3B-centered network or random selected-gene network for link removal fraction *f*. All quantities are averaged over 1,000 realizations for each network (left). The bar graphs represent the link removal faction at $f = 0.6$ in the KDM3B-centered network and randomly selected gene network (right). Data are represented as the mean ± SD.

(F) H3K9 methylation-dependent heterochromatin dynamics by the KDM3B during aging of terminally differentiated retinal cone cells.

See also Figure S11.

The epigenetic hallmark of heterochromatin is H3K9me2/3 at repetitive non-coding sequences such as pericentric satellites and subtelomeric repeats that are silenced and clustered forming constitutive heterochromatin.[9] However, recent work shows that H3K9 methylation has more dynamic function in the repression of tissue-specific genes at facultative heterochromatin (f-het).[4] Dynamic interplay between KMTs and KDMs that target H3K9 has a unique functional role in forming f-het, which controls lineage-specific gene repression during development in a tissue-specific manner.[6,40] Maintenance of H3K9 methylation signatures is required to prevent non-lineage gene expression during neurogenesis. Loss of SETDB1 in the neuronal lineage impairs the differentiation of neurons and increases the chances of neuronal precursor cells developing into astrocytes.[41] Postnatal depletion of G9A led to the activation of non-neuronal and progenitor genes that resulted in behavior phenotypes.[42] Although the importance of H3K9 methylation-mediated heterochromatin features by KMTs is elucidated in tissue organogenesis and differentiation, the interplay between KMTs and KDMs at H3K9 methylation was not revealed yet. Also, how silenced tissue-specific genes at facultative heterochromatin during early development can be activated in differentiated cells through the exit from the heterochromatin? We found that KDM3B specifically demethylates H3K9me1/2 of neuronal lineage genes involved in synapse function during terminal differentiation of cone photoreceptors in the retina. The enzymatic activity of KDM3B was maintained during lifetime, but the expression level of *Kdm3b* decreased gradually during aging (Figure 7F). By the reduction of KDM3B, cell type-specific genes were located at the euchromatic region and changed their position to the heterochromatin region. These results show that KDM3B is required for the maintenance of cell type-specific gene expression by generating the transcriptional barrier from the facultative heterochromatin region (Figure 7F).

GRNs affect all biological phenomena associated with maturation (development), rapid destruction (disease), and slow destruction (aging) (Figure 7). In terms of network topology, conventional GRNs cannot discriminate subtle differences, such as environmental adverse effects and aging. We suggest that the integration of multi-dimensional epigenomic networks and GRNs will help improve the understanding of biological phenomena by allowing for the measurement of network strength during aging. We focused on an epigenetic regulator (KDM3B)-centered network during retinal aging (Figure 7). Even though many studies have investigated epigenetic regulation in cancers or stem cells, the precise mechanism of epigenomic modification in completely differentiated and aging cells is largely unknown. KDM3B is an H3K9me1 and H3K9me2 demethylase that belongs to the KDM3 family and acts as a transcriptional activator.[14,15] KDM3B has been shown to accelerate leukemogenesis by regulating lmo2 expression via the reduction of H3K9me2 methylation.[15] Additionally, the demethylation activity of KDM3A/B activates Wnt target genes, which increase the survival of human colorectal cancer stem cells.[30] We established *Kdm3b*$^{+/-}$ mice and demonstrated the functional roles of KDM3B via morphological and physiological changes, as well as genome-wide transcriptional and epigenomic analysis during retinal aging. Importantly, these data suggest that site-specific changes of H3K9 methylation in *Kdm3b*$^{+/-}$ mice accelerate the destruction of GRN and lead to the "loss or gain of heterochromatin features" affecting cellular lifespan depending on the organism. Furthermore, we constructed the KDM3B-centered GRN using integrated RNA-seq and ChIP-seq analysis, which showed that the strength of network between a transcriptional regulator and its target genes weakened in *Kdm3b*$^{+/-}$ mice. Although the network structural properties are not significantly different between *Kdm3b*$^{+/+}$ and *Kdm3b*$^{+/-}$ mice (Figure S11D), we found interior topological differences by measuring network dissimilarity and robustness (Figures 7D and 7E). Surprisingly, the network dissimilarity between 18-month-old *Kdm3b*$^{+/+}$ and 12-month-old *Kdm3b*$^{+/-}$ mice appeared relatively close. These results suggest that the changes observed in *Kdm3b*$^{+/-}$ mice reflect those that occur in normal aging. Eventually, *Kdm3b* haploinsufficiency diminished the structural gene network via heterochromatin misregulation and induced cascading destruction of network integrity. In the scope of molecular biology, these delicate alterations emerged as post-transcriptional and translational regulation. For example, disrupted alternative splicing of the *CPSF1* and *CNOT3* genes leads to the attenuation of biological processes in retinitis pigmentosa.[43] We identified the retained intron events on the *Aldoa* gene in *Kdm3b*$^{+/-}$ mouse retinas (Figure S4K). This result suggests that *Kdm3b* haploinsufficiency changes the normal transcriptome profile, which is a potential cause of retinal disease via post-transcriptional regulation during aging.

Cell type-specific gene regulation in retinas during development, differentiation, and aging processes has been of interest for a long time in the field of neurodevelopmental biology. Since retinal neurogenesis is driven by synergistic actions of transcription factors, which are expressed across several cell subtypes or specific cell types throughout development, it is difficult to detect the transcripts with rare cell type signatures in individual cells through bulk RNA-seq. Gene expression signatures of one cell type may be hidden by complementary patterns in other cell types. The recent advent of single-cell next-generation sequencing-based methods has enabled defining cellular identity and heterogeneity within populations through molecular classification, comparative taxonomy, and stratification of molecular heterogeneity.[44] We found that the distribution of heterochromatin was altered in cone photoreceptors during retinal aging (Figure 1). This result raised the possibility that a chromatin remodeler is required for the organization of chromatin structure during retinal aging. To identify the key regulator in cone photoreceptors, we employed single-cell transcriptomics during retinal cell aging. The mRNA expression of *Kdm3b* between rod and cone photoreceptors was similar in aged mouse retinas (Figure S2C). We further introduced a method to explain mRNA stability in each single cell through the "RNA velocity" concept and measured the stability of mRNA molecules in each single cell generated from scRNA-seq. Surprisingly, we observed that the mRNA stability of *Kdm3b* was regulated differentially in cone and rod photoreceptors depending on the cell types. It was confirmed that the stability of *Kdm3b* was relatively weakened with cellular aging in the cone cells (Figure 2E). Through the

introduction of the "RNA velocity" concept and in combination with scRNA-seq data, we could measure the subtle changes in mRNA stability and could extrapolate the results to address the cell type-specific neuronal aging issue, which is difficult to explain only by changes in gene expression. In this study, for the first time, we clarified the aspects of the transcriptome using scRNA-seq that were changed during the aging process in retinal cells and analyzed the changes at different ages in an integrated system.

Rising evidence suggested that epigenetic modulators often exhibit dual function, both activator and repressor, in gene transcriptional regulation, development, and cancer progression. However, how these dual functions are coordinated in specific cellular contexts remains incompletely understood. In this aspect, it is interesting that KDM3B, an active histone demethylase, unexpectedly activates apoptotic genes through the loss of heterochromatin in aged *Kdm3b*$^{+/-}$ mice retinas. Since KDM3B lacks the DNA-binding ability, it may require transcription factor to have a potential for the gene set-specific regulation. Consistent with this hypothesis, our RNA-seq analysis supported an increasing expression pattern of AP-1 family transcription factors during retinal aging. In addition, motif analysis of KDM3B ChIP-seq data uncovered a list of transcription factors that associate with KDM3B to specific target genes. In particular, KDM3B peaks carry a motif predicted by AP-1 family transcription factors such as c-Fos and JUNB. We demonstrated that KDM3B co-occupies a subset of KDM3B target genes via physical interaction; it remains to be determined if this interaction is direct or indirect (Figure 7C). The immediate-early gene *c-fos* is expressed in various cell types by numerous stimuli and conditions. c-Fos is well known to dimerize with c-Jun family proteins, which are a major component of the AP-1 transcriptional complex and induced cell death in several types of neuronal cells.[45–47] c-Fos is also required for both regenerations of retina ganglion cells and apoptotic cell death.[48] Consistent with previous results, we observed that c-Fos and JUNB are associated with KDM3B at the regulatory regions of apoptotic genes and synapse assembly genes in mice retina. It supports that c-Fos and JUNB might fine-tune transcription of KDM3B target genes as acting an on-off switch during aging (Figure S11F). Although it remains to discover detailed mechanisms, our data provide an important resource for elucidating novel aging regulatory mechanisms through heterochromatin reorganization.

In summary, our findings provide new insight into how site-specific epigenetic regulation in a specific cell type contributes to the maintenance of heterochromatic homeostasis. We demonstrated an epigenomic network in the retina, which might illuminate the selective roles of KDM3B in synaptic transmission and apoptotic signaling pathways during retinal aging. We integrated epigenomic network analysis with physiological and morphological analyses of the *Kdm3b*$^{+/-}$ mouse retina. Ablation of *Kdm3b* results in presynaptic cone abnormalities by inducing apoptotic signals. *Kdm3b* haploinsufficiency downregulates a subset of synapse assembly genes, with H3K9 methylation-associated silencing. Overall, these findings suggest that integrating genomic and epigenomic data in network studies helps predict whether subtle changes in network strength increase susceptibility to age-related neuronal disease.

Limitations of the study

Although the present study revealed the epigenome-wide regulation of KDM3B in the aging mouse retina, there are still some limitations that need to be addressed. The single-cell RNA-seq data showed KDM3B mRNA expressed in various retinal cell types, including rod photoreceptors and bipolar cells. However, KDM3B protein was found to be highly enriched in cone photoreceptors and negligible in other cell types. We explained this discrepancy using the mRNA stability concept represented as mRNA velocity. In the future, it would be beneficial to identify the roles of unstable mRNA in cones related to KDM3B protein expression and function. We also discovered epigenomic imbalances in cell type-specific genes and apoptotic cell death genes during the aging of differentiated retinal cells. Moving forward, we will continue to investigate the disruption of epigenomic homeostasis through proper 3D chromatin organization in aging and disease mechanisms.

STAR★METHODS

Detailed methods are provided in the online version of this paper and include the following:

- KEY RESOURCES TABLE
- RESOURCE AVAILABILITY
  - Lead contact
  - Materials availability
  - Data and code availability
- EXPERIMENTAL MODEL AND STUDY PARTICIPANT DETAILS
  - Expression strains
- METHOD DETAILS
  - Immunohistochemistry (IHC)
  - Retinal dissection and dissociation
  - Single cell library preparation
  - Single-cell RNA sequencing (scRNA-seq)
  - Bioinformatics processing for scRNA-seq analysis
  - Clustering analysis and final cell type assignment
  - Estimating mRNA stability in cells
  - Immunoprecipitation and immunoblot
  - AAV viral vector production and subretinal injection

- Total RNA isolation and RT-qPCR
- Electroretinogram (ERG)
- Transmission electron microscopic (TEM) analyses
- RNA sequencing and bioinformatical analysis
- Chromatin immunoprecipitation (ChIP) sequencing
- ChIP-seq library preparation and bioinformatical analysis
- Motif discovery
- Gene ontology and GSEA analysis
- Epigenomic network construction
- Measurement of network structural dissimilarities

● QUANTIFICATION AND STATISTICAL ANALYSIS

- Image analysis
- Statistical analysis

SUPPLEMENTAL INFORMATION

Supplemental information can be found online at https://doi.org/10.1016/j.isci.2024.110380.

ACKNOWLEDGMENTS

The study was supported by Korea Environment Industry & Technology Institute (KEITI) through "Digital Infrastructure Building Project for Monitoring, Surveying and Evaluating the Environmental Health Program" (grant and award number: 2021003330007) funded by Korea Ministry of Environment (MOE). This work also supported by the National Research Foundation of Korea (NRF) grant funded by the Korea government (MIST) (Basic Research Laboratory: NRF-RS-2023-00220089; NRF-2023R1A2C1007657). *Kdm3b* heterozygote mouse was kindly gifted from Prof. Sang-Beom Seo (Chung-Ang University, South Korea). We also thank Prof. Yong-Seok Lee (Seoul National University, Seoul, South Korea) and Prof. Sung Hyun Kim (Kyung Hee University, Seoul, South Korea) for the scientific comments of synaptic functions of the neurons.

AUTHOR CONTRIBUTIONS

Overall scientific conceptualization, J.-W.K.; methodology and investigation, M.-J.A., J.-Y.K., Jinho Kim, D.-H.K., G.-S.S., H.-M.L., A.-R.J., Y.P., Y.H., C.-H.K., M.J.K., and J.-W.K.; data analysis and scientific comments, M.-J.A., J.-Y.K., Jinho Kim, D.-H.K., Y.-S.J., Jeongkyu Kim, S.R., S.-B.S., and J.-W.K.; statistical and bioinformatical analysis, Jinho Kim, Y.H., J.-Y.K., and J.-W.K.; writing – original draft, M.-J.A., J.-Y.K., Jinho Kim, and J.-W.K.; funding acquisition, J.-W.K.; supervision and project administration, J.-W.K.

DECLARATION OF INTERESTS

The authors declare no competing interests.

Received: August 7, 2023
Revised: March 14, 2024
Accepted: June 24, 2024
Published: June 26, 2024

REFERENCES

1. Klemm, S.L., Shipony, Z., and Greenleaf, W.J. (2019). Chromatin accessibility and the regulatory epigenome. Nat. Rev. Genet. *20*, 207–220. https://doi.org/10.1038/s41576-018-0089-8.
2. Ninova, M., Fejes Toth, K., and Aravin, A.A. (2019). The control of gene expression and cell identity by H3K9 trimethylation. Development *146*, dev181180. https://doi.org/10.1242/dev.181180.
3. Trojer, P., and Reinberg, D. (2007). Facultative heterochromatin: is there a distinctive molecular signature? Mol. Cell *28*, 1–13. https://doi.org/10.1016/j.molcel.2007.09.011.
4. Methot, S.P., Padeken, J., Brancati, G., Zeller, P., Delaney, C.E., Gaidatzis, D., Kohler, H., van Oudenaarden, A., Grosshans, H., and Gasser, S.M. (2021). H3K9me selectively blocks transcription factor activity and ensures differentiated tissue integrity. Nat. Cell Biol. *23*, 1163–1175. https://doi.org/10.1038/s41556-021-00776-w.
5. Nicetto, D., Donahue, G., Jain, T., Peng, T., Sidoli, S., Sheng, L., Montavon, T., Becker, J.S., Grindheim, J.M., Blahnik, K., et al. (2019). H3K9me3-heterochromatin loss at protein-coding genes enables developmental lineage specification. Science *363*, 294–297. https://doi.org/10.1126/science.aau0583.
6. Becker, J.S., Nicetto, D., and Zaret, K.S. (2016). H3K9me3-Dependent Heterochromatin: Barrier to Cell Fate Changes. Trends Genet. *32*, 29–41. https://doi.org/10.1016/j.tig.2015.11.001.
7. Nicetto, D., and Zaret, K.S. (2019). Role of H3K9me3 heterochromatin in cell identity establishment and maintenance. Curr. Opin. Genet. Dev. *55*, 1–10. https://doi.org/10.1016/j.gde.2019.04.013.
8. Yang, J.H., Hayano, M., Griffin, P.T., Amorim, J.A., Bonkowski, M.S., Apostolides, J.K., Salfati, E.L., Blanchette, M., Munding, E.M., Bhakta, M., et al. (2023). Loss of epigenetic information as a cause of mammalian aging. Cell *186*, 305–326.e27. https://doi.org/10.1016/j.cell.2022.12.027.
9. Padeken, J., Methot, S.P., and Gasser, S.M. (2022). Establishment of H3K9-methylated heterochromatin and its functions in tissue differentiation and maintenance. Nat. Rev. Mol. Cell Biol. *23*, 623–640. https://doi.org/10.1038/s41580-022-00483-w.
10. Keenan, C.R., Iannarella, N., Naselli, G., Bediaga, N.G., Johanson, T.M., Harrison, L.C., and Allan, R.S. (2020). Extreme disruption of heterochromatin is required for

accelerated hematopoietic aging. Blood *135*, 2049–2058. https://doi.org/10.1182/blood.2019002990.
11. Montavon, T., Shukeir, N., Erikson, G., Engist, B., Onishi-Seebacher, M., Ryan, D., Musa, Y., Mittler, G., Meyer, A.G., Genoud, C., and Jenuwein, T. (2021). Complete loss of H3K9 methylation dissolves mouse heterochromatin organization. Nat. Commun. *12*, 4359. https://doi.org/10.1038/s41467-021-24532-8.
12. Mosammaparast, N., and Shi, Y. (2010). Reversal of histone methylation: biochemical and molecular mechanisms of histone demethylases. Annu. Rev. Biochem. *79*, 155–179. https://doi.org/10.1146/annurev.biochem.78.070907.103946.
13. Kooistra, S.M., and Helin, K. (2012). Molecular mechanisms and potential functions of histone demethylases. Nat. Rev. Mol. Cell Biol. *13*, 297–311. https://doi.org/10.1038/nrm3327.
14. Krieg, A.J., Rankin, E.B., Chan, D., Razorenova, O., Fernandez, S., and Giaccia, A.J. (2010). Regulation of the histone demethylase JMJD1A by hypoxia-inducible factor 1 alpha enhances hypoxic gene expression and tumor growth. Mol. Cell Biol. *30*, 344–353. https://doi.org/10.1128/MCB.00444-09.
15. Kim, J.Y., Kim, K.B., Eom, G.H., Choe, N., Kee, H.J., Son, H.J., Oh, S.T., Kim, D.W., Pak, J.H., Baek, H.J., et al. (2012). KDM3B is the H3K9 demethylase involved in transcriptional activation of lmo2 in leukemia. Mol. Cell Biol. *32*, 2917–2933. https://doi.org/10.1128/MCB.00133-12.
16. Yamane, K., Toumazou, C., Tsukada, Y., Erdjument-Bromage, H., Tempst, P., Wong, J., and Zhang, Y. (2006). JHDM2A, a JmjC-containing H3K9 demethylase, facilitates transcription activation by androgen receptor. Cell *125*, 483–495. https://doi.org/10.1016/j.cell.2006.03.027.
17. An, M.J., Kim, D.H., Kim, C.H., Kim, M., Rhee, S., Seo, S.B., and Kim, J.W. (2019). Histone demethylase KDM3B regulates the transcriptional network of cell-cycle genes in hepatocarcinoma HepG2 cells. Biochem. Biophys. Res. Commun. *508*, 576–582. https://doi.org/10.1016/j.bbrc.2018.11.179.
18. Peter, I.S., and Davidson, E.H. (2011). Evolution of gene regulatory networks controlling body plan development. Cell *144*, 970–985. https://doi.org/10.1016/j.cell.2011.02.017.
19. Davidson, E.H., and Levine, M.S. (2008). Properties of developmental gene regulatory networks. Proc. Natl. Acad. Sci. USA *105*, 20063–20066. https://doi.org/10.1073/pnas.0806007105.
20. Kim, J.W., Yang, H.J., Brooks, M.J., Zelinger, L., Karakulah, G., Gotoh, N., Boleda, A., Gieser, L., Giuste, F., Whitaker, D.T., et al. (2016). NRL-Regulated Transcriptome Dynamics of Developing Rod Photoreceptors. Cell Rep. *17*, 2460–2473. https://doi.org/10.1016/j.celrep.2016.10.074.
21. Kim, Y.G., Bak, M.S., Kim, A., Kim, Y., Chae, Y.C., Kim, Y.L., Chun, Y.S., An, J.Y., Seo, S.B., Kim, S.J., and Lee, Y.S. (2021). Kdm3b haploinsufficiency impairs the consolidation of cerebellum-dependent motor memory in mice. Mol. Brain *14*, 106. https://doi.org/10.1186/s13041-021-00815-5.
22. Polanski, K., Young, M.D., Miao, Z., Meyer, K.B., Teichmann, S.A., and Park, J.E. (2020). BBKNN: fast batch alignment of single cell transcriptomes. Bioinformatics *36*, 964–965. https://doi.org/10.1093/bioinformatics/btz625.
23. Shekhar, K., Lapan, S.W., Whitney, I.E., Tran, N.M., Macosko, E.Z., Kowalczyk, M., Adiconis, X., Levin, J.Z., Nemesh, J., Goldman, M., et al. (2016). Comprehensive Classification of Retinal Bipolar Neurons by Single-Cell Transcriptomics. Cell *166*, 1308–1323.e30. https://doi.org/10.1016/j.cell.2016.07.054.
24. Lukowski, S.W., Lo, C.Y., Sharov, A.A., Nguyen, Q., Fang, L., Hung, S.S., Zhu, L., Zhang, T., Grunert, U., Nguyen, T., et al. (2019). A single-cell transcriptome atlas of the adult human retina. EMBO J. *38*, e100811. https://doi.org/10.15252/embj.2018100811.
25. Yan, W., Peng, Y.R., van Zyl, T., Regev, A., Shekhar, K., Juric, D., and Sanes, J.R. (2020). Cell Atlas of The Human Fovea and Peripheral Retina. Sci. Rep. *10*, 9802. https://doi.org/10.1038/s41598-020-66092-9.
26. La Manno, G., Soldatov, R., Zeisel, A., Braun, E., Hochgerner, H., Petukhov, V., Lidschreiber, K., Kastriti, M.E., Lonnerberg, P., Furlan, A., et al. (2018). RNA velocity of single cells. Nature *560*, 494–498. https://doi.org/10.1038/s41586-018-0414-6.
27. Bergen, V., Soldatov, R.A., Kharchenko, P.V., and Theis, F.J. (2021). RNA velocity-current challenges and future perspectives. Mol. Syst. Biol. *17*, e10282. https://doi.org/10.15252/msb.202110282.
28. Gupta, K., Yadav, P., Maryam, S., Ahuja, G., and Sengupta, D. (2021). Quantification of Age-Related Decline in Transcriptional Homeostasis. J. Mol. Biol. *433*, 167179. https://doi.org/10.1016/j.jmb.2021.167179.
29. Kim, J.W., Yang, H.J., Oel, A.P., Brooks, M.J., Jia, L., Plachetzki, D.C., Li, W., Allison, W.T., and Swaroop, A. (2016). Recruitment of Rod Photoreceptors from Short-Wavelength-Sensitive Cones during the Evolution of Nocturnal Vision in Mammals. Dev. Cell *37*, 520–532. https://doi.org/10.1016/j.devcel.2016.05.023.
30. Li, J., Yu, B., Deng, P., Cheng, Y., Yu, Y., Kevork, K., Ramadoss, S., Ding, X., Li, X., and Wang, C.Y. (2017). KDM3 epigenetically controls tumorigenic potentials of human colorectal cancer stem cells through Wnt/β-catenin signalling. Nat. Commun. *8*, 15146. https://doi.org/10.1038/ncomms15146.
31. Shi, Y. (2007). Histone lysine demethylases: emerging roles in development, physiology and disease. Nat. Rev. Genet. *8*, 829–833. https://doi.org/10.1038/nrg2218.
32. Abler, A.S., Chang, C.J., Ful, J., Tso, M.O., and Lam, T.T. (1996). Photic injury triggers apoptosis of photoreceptor cells. Res. Commun. Mol. Pathol. Pharmacol. *92*, 177–189.
33. Curcio, C.A., Medeiros, N.E., and Millican, C.L. (1996). Photoreceptor loss in age-related macular degeneration. Invest. Ophthalmol. Vis. Sci. *37*, 1236–1249.
34. Fischer, A.J., and Reh, T.A. (2001). Müller glia are a potential source of neural regeneration in the postnatal chicken retina. Nat. Neurosci. *4*, 247–252. https://doi.org/10.1038/85090.
35. Baden, T., Euler, T., Weckstrom, M., and Lagnado, L. (2013). Spikes and ribbon synapses in early vision. Trends Neurosci. *36*, 480–488. https://doi.org/10.1016/j.tins.2013.04.006.
36. Schieber, T.A., Carpi, L., Diaz-Guilera, A., Pardalos, P.M., Masoller, C., and Ravetti, M.G. (2017). Quantification of network structural dissimilarities. Nat. Commun. *8*, 13928. https://doi.org/10.1038/ncomms13928.
37. Dehmer, M., and Emmert-Streib, F. (2018). Comments to "Quantification of network structural dissimilarities" published by Schieber et al. Math. Methods Appl. Sci. *41*, 5711–5713.
38. Barabási, A.-L. (2016). Network Science (Cambridge university press).
39. Cohen, R., Erez, K., ben-Avraham, D., and Havlin, S. (2000). Resilience of the internet to random breakdowns. Phys. Rev. Lett. *85*, 4626–4628. https://doi.org/10.1103/PhysRevLett.85.4626.
40. McCarthy, R.L., Zhang, J., and Zaret, K.S. (2023). Diverse heterochromatin states restricting cell identity and reprogramming. Trends Biochem. Sci. *48*, 513–526. https://doi.org/10.1016/j.tibs.2023.02.007.
41. Tan, S.L., Nishi, M., Ohtsuka, T., Matsui, T., Takemoto, K., Kamio-Miura, A., Aburatani, H., Shinkai, Y., and Kageyama, R. (2012). Essential roles of the histone methyltransferase ESET in the epigenetic control of neural progenitor cells during development. Development *139*, 3806–3816. https://doi.org/10.1242/dev.082198.
42. Schaefer, A., Sampath, S.C., Intrator, A., Min, A., Gertler, T.S., Surmeier, D.J., Tarakhovsky, A., and Greengard, P. (2009). Control of cognition and adaptive behavior by the GLP/G9a epigenetic suppressor complex. Neuron *64*, 678–691. https://doi.org/10.1016/j.neuron.2009.11.019.
43. Buskin, A., Zhu, L., Chichagova, V., Basu, B., Mozaffari-Jovin, S., Dolan, D., Droop, A., Collin, J., Bronstein, R., Mehrotra, S., et al. (2018). Disrupted alternative splicing for genes implicated in splicing and ciliogenesis causes PRPF31 retinitis pigmentosa. Nat. Commun. *9*, 4234. https://doi.org/10.1038/s41467-018-06448-y.
44. Peng, Y.R., Shekhar, K., Yan, W., Herrmann, D., Sappington, A., Bryman, G.S., van Zyl, T., Do, M.T.H., Regev, A., and Sanes, J.R. (2019). Molecular Classification and Comparative Taxonomics of Foveal and Peripheral Cells in Primate Retina. Cell *176*, 1222–1237.e22. https://doi.org/10.1016/j.cell.2019.01.004.
45. Curran, T., and Morgan, J.I. (1995). Fos: an immediate-early transcription factor in neurons. J. Neurobiol. *26*, 403–412. https://doi.org/10.1002/neu.480260312.
46. Smeyne, R.J., Vendrell, M., Hayward, M., Baker, S.J., Miao, G.G., Schilling, K., Robertson, L.M., Curran, T., and Morgan, J.I. (1993). Continuous c-fos expression precedes programmed cell death *in vivo*. Nature *363*, 166–169. https://doi.org/10.1038/363166a0.
47. Hafezi, F., Steinbach, J.P., Marti, A., Munz, K., Wang, Z.Q., Wagner, E.F., Aguzzi, A., and Reme, C.E. (1997). The absence of c-fos prevents light-induced apoptotic cell death of photoreceptors in retinal degeneration *in vivo*. Nat. Med. *3*, 346–349. https://doi.org/10.1038/nm0397-346.
48. Oshitari, T., Dezawa, M., Okada, S., Takano, M., Negishi, H., Horie, H., Sawada, H., Tokuhisa, T., and Adachi-Usami, E. (2002). The role of c-fos in cell death and regeneration of retinal ganglion cells. Invest. Ophthalmol. Vis. Sci. *43*, 2442–2449.
49. Dobin, A., Davis, C.A., Schlesinger, F., Drenkow, J., Zaleski, C., Jha, S., Batut, P., Chaisson, M., and Gingeras, T.R. (2013). STAR: ultrafast universal RNA-seq aligner. Bioinformatics *29*, 15–21. https://doi.org/10.1093/bioinformatics/bts635.
50. Li, B., and Dewey, C.N. (2011). RSEM: accurate transcript quantification from RNA-Seq data with or without a reference genome.

BMC Bioinf. *12*, 323. https://doi.org/10.1186/1471-2105-12-323.

51. Love, M.I., Huber, W., and Anders, S. (2014). Moderated estimation of fold change and dispersion for RNA-seq data with DESeq2. Genome Biol. *15*, 550. https://doi.org/10.1186/s13059-014-0550-8.
52. Robinson, M.D., McCarthy, D.J., and Smyth, G.K. (2010). edgeR: a Bioconductor package for differential expression analysis of digital gene expression data. Bioinformatics *26*, 139–140. https://doi.org/10.1093/bioinformatics/btp616.
53. Langmead, B., and Salzberg, S.L. (2012). Fast gapped-read alignment with Bowtie 2. Nat. Methods *9*, 357–359. https://doi.org/10.1038/nmeth.1923.
54. Stovner, E.B., and Saetrom, P. (2019). epic2 efficiently finds diffuse domains in ChIP-seq data. Bioinformatics *35*, 4392–4393. https://doi.org/10.1093/bioinformatics/btz232.
55. Heinz, S., Benner, C., Spann, N., Bertolino, E., Lin, Y.C., Laslo, P., Cheng, J.X., Murre, C., Singh, H., and Glass, C.K. (2010). Simple combinations of lineage-determining transcription factors prime cis-regulatory elements required for macrophage and B cell identities. Mol. Cell *38*, 576–589. https://doi.org/10.1016/j.molcel.2010.05.004.
56. Huang da, W., Sherman, B.T., and Lempicki, R.A. (2009). Systematic and integrative analysis of large gene lists using DAVID bioinformatics resources. Nat. Protoc. *4*, 44–57. https://doi.org/10.1038/nprot.2008.211.
57. Supek, F., Bosnjak, M., Skunca, N., and Smuc, T. (2011). REVIGO summarizes and visualizes long lists of gene ontology terms. PLoS One *6*, e21800. https://doi.org/10.1371/journal.pone.0021800.
58. Subramanian, A., Tamayo, P., Mootha, V.K., Mukherjee, S., Ebert, B.L., Gillette, M.A., Paulovich, A., Pomeroy, S.L., Golub, T.R., Lander, E.S., and Mesirov, J.P. (2005). Gene set enrichment analysis: a knowledge-based approach for interpreting genome-wide expression profiles. Proc. Natl. Acad. Sci. USA *102*, 15545–15550. https://doi.org/10.1073/pnas.0506580102.
59. Shen, S., Park, J.W., Lu, Z.X., Lin, L., Henry, M.D., Wu, Y.N., Zhou, Q., and Xing, Y. (2014). rMATS: robust and flexible detection of differential alternative splicing from replicate RNA-Seq data. Proc. Natl. Acad. Sci. USA *111*, E5593–E5601. https://doi.org/10.1073/pnas.1419161111.
60. Middleton, R., Gao, D., Thomas, A., Singh, B., Au, A., Wong, J.J., Bomane, A., Cosson, B., Eyras, E., Rasko, J.E., and Ritchie, W. (2017). IRFinder: assessing the impact of intron retention on mammalian gene expression. Genome Biol. *18*, 51. https://doi.org/10.1186/s13059-017-1184-4.
61. Wolf, F.A., Angerer, P., and Theis, F.J. (2018). SCANPY: large-scale single-cell gene expression data analysis. Genome Biol. *19*, 15. https://doi.org/10.1186/s13059-017-1382-0.
62. Bergen, V., Lange, M., Peidli, S., Wolf, F.A., and Theis, F.J. (2020). Generalizing RNA velocity to transient cell states through dynamical modeling. Nat. Biotechnol. *38*, 1408–1414. https://doi.org/10.1038/s41587-020-0591-3.
63. Danecek, P., Bonfield, J.K., Liddle, J., Marshall, J., Ohan, V., Pollard, M.O., Whitwham, A., Keane, T., McCarthy, S.A., Davies, R.M., and Li, H. (2021). Twelve years of SAMtools and BCFtools. GigaScience *10*, giab008. https://doi.org/10.1093/gigascience/giab008.
64. Quinlan, A.R., and Hall, I.M. (2010). BEDTools: a flexible suite of utilities for comparing genomic features. Bioinformatics *26*, 841–842. https://doi.org/10.1093/bioinformatics/btq033.
65. Robinson, J.T., Thorvaldsdottir, H., Winckler, W., Guttman, M., Lander, E.S., Getz, G., and Mesirov, J.P. (2011). Integrative genomics viewer. Nat. Biotechnol. *29*, 24–26. https://doi.org/10.1038/nbt.1754.
66. Zheng, G.X., Terry, J.M., Belgrader, P., Ryvkin, P., Bent, Z.W., Wilson, R., Ziraldo, S.B., Wheeler, T.D., McDermott, G.P., Zhu, J., et al. (2017). Massively parallel digital transcriptional profiling of single cells. Nat. Commun. *8*, 14049. https://doi.org/10.1038/ncomms14049.
67. Wolock, S.L., Lopez, R., and Klein, A.M. (2019). Scrublet: Computational Identification of Cell Doublets in Single-Cell Transcriptomic Data. Cell Syst. *8*, 281–291.e9. https://doi.org/10.1016/j.cels.2018.11.005.
68. van Dijk, D., Sharma, R., Nainys, J., Yim, K., Kathail, P., Carr, A.J., Burdziak, C., Moon, K.R., Chaffer, C.L., Pattabiraman, D., et al. (2018). Recovering Gene Interactions from Single-Cell Data Using Data Diffusion. Cell *174*, 716–729.e27. https://doi.org/10.1016/j.cell.2018.05.061.
69. Hoh Kam, J., Lenassi, E., Malik, T.H., Pickering, M.C., and Jeffery, G. (2013). Complement component C3 plays a critical role in protecting the aging retina in a murine model of age-related macular degeneration. Am. J. Pathol. *183*, 480–492. https://doi.org/10.1016/j.ajpath.2013.04.008.
70. Malik, A.N., Vierbuchen, T., Hemberg, M., Rubin, A.A., Ling, E., Couch, C.H., Stroud, H., Spiegel, I., Farh, K.K., Harmin, D.A., and Greenberg, M.E. (2014). Genome-wide identification and characterization of functional neuronal activity-dependent enhancers. Nat. Neurosci. *17*, 1330–1339. https://doi.org/10.1038/nn.3808.
71. Zhou, Y., Zhou, B., Pache, L., Chang, M., Khodabakhshi, A.H., Tanaseichuk, O., Benner, C., and Chanda, S.K. (2019). Metascape provides a biologist-oriented resource for the analysis of systems-level datasets. Nat. Commun. *10*, 1523. https://doi.org/10.1038/s41467-019-09234-6.
72. Zhou, G., Soufan, O., Ewald, J., Hancock, R.E.W., Basu, N., and Xia, J. (2019). NetworkAnalyst 3.0: a visual analytics platform for comprehensive gene expression profiling and meta-analysis. Nucleic Acids Res. *47*, W234–W241. https://doi.org/10.1093/nar/gkz240.

STAR★METHODS

KEY RESOURCES TABLE

REAGENT or RESOURCE	SOURCE	IDENTIFIER
Antibodies		
Cy™3 AffiniPure Goat Anti-Rabbit IgG (H+L)	Jackson Immunoresearch	Cat 111-165-144, Lot 143018; RRID: AB_2338006
Fluorescein (FITC) AffiniPure Donkey Anti-Mouse IgG (H+L)	Jackson Immunoresearch	Cat 715-095-150, Lot 141614; RRID: AB_2340792
Mouse monoclonal anti-CtBP2	BD biosciences	Cat #612044, Lot 7208971; RRID: AB_399431
Mouse monoclonal anti-Cytochrome c	Santa cruz	Cat sc-13156, Lot a1618; RRID: AB_627385
Mouse monoclonal anti-Rhodopsin	Invitrogen	Cat P21940, Lot 1899760; RRID: AB_2539827
Mouse monoclonal anti-β-Actin	Santa cruz	Cat sc-47778, Lot e1017; RRID: AB_626632
Rabbit IgG isotype control	GeneTex	Cat GTX35035, Lot 821904736; RRID: AB_10623175
Rabbit polyclonal anti-Cone Arrestin	Merck	Cat ab15282, Lot 2802590; RRID: AB_1163387
Rabbit polyclonal anti-GFAP	Dako	Cat Z0334; RRID: AB_10013382
Rabbit polyclonal anti-H3K9me1	Abcam	Cat ab9045, Lot GR3303087-1; RRID: AB_306963
Rabbit polyclonal anti-H3K9me2	Abcam	Cat ab17688, Lot GR17938-5
Rabbit polyclonal anti-H3K9me3	Abcam	Cat ab8898, Lot GR3281994-1; RRID: AB_306848
Rabbit polyclonal anti-KDM3B	Cell Signaling Technology	Cat #2621s; RRID: AB_915946
Rabbit polyclonal anti-c-Fos	Cell Signaling Technology	Cat #2250; RRID: AB_2247211
Rabbit polyclonal anti-SCGN	Novus biologicals	NBP2-20286, Lot 40415
Rabbit polyclonal anti-CHX10	GeneTex	Cat GTX114143; RRID: AB_11161878
Rabbit polyclonal anti-PRKCA	Sigma-Aldrich	Cat P4334, Lot 118M4864V; RRID: AB_477345
Rabbit polyclonal anti-JUNB	Santa cruz	Cat sc-46; RRID: AB_2130022
Rabbit polyclonal anti-Calbindin D-28K	Sigma-Aldrich	Cat PC253L, Lot 3384068; RRID: AB_213554
Mouse monoclonal anti-BRN3A	Santa cruz	Cat Sc-8429, Lot F1510; RRID: AB_626765
Bacterial and virus strains		
pAAV[Exp]-CMV>EGFP:WPRE (VB010000-9394npt)	Vectorbuilder	AAV7m8M(VB010000-9394npt)-C
pAAV[Exp]-CMV>{mKDM3B ATG+AAAG+E15-24}/T2A/EGFP (VB220616-1503xny)	Vectorbuilder	AAV7m8M(VB220616-1503xny)-K1
pAAV[shRNA]-EGFPU6>Scramble_shRNA (VB010000- 0023jze)	Vectorbuilder	AAV7m8M(VB010000-0023jze)-C
pAAV[shRNA]-EGFP-U6>{mKdm3b E19} (VB220616-1495pmh)	Vectorbuilder	AAV7m8M(VB220616-1495pmh)-K1
Biological samples		
Mouse Retinas	This paper	N/A
Chemicals, peptides, and recombinant proteins		
2-propanol	SIGMA	19516
4′,6-Diamidino-2-phenylindole dihydrochloride (DAPI)	SIGMA	D8417
Agarose	Mp Biomedicals	AGAH0500
Chloroform	SIGMA	107024
Ethanol	Merck	100983
Glycogen	SIGMA	10901393001
Goat serum	Life Technologies	16210-064
Methanol	Merck	107018

(*Continued on next page*)

Continued

REAGENT or RESOURCE	SOURCE	IDENTIFIER
OCT compound	SAKURA	4583
Paraformaldehyde	Electron Microscopy Sciences	15710
Phenol:Chloroform:Isoamyl alcohol	Thermo Scientific	15593-049
PMSF	Thermo Scientific	36978
Protease inhibitor cocktail	Roche	11836153001
Protein A/G magnet beads	Thermo Scientific	26162
Proteinase K	Roche	3115828001
Sodium azide	SIGMA	S0489
Tribromoethanol	Sigma	T48402
Triton X-100	Mp Biomedicals	04807423
TRIzol solution	Invitrogen	15596018
Critical commercial assays		
POWER SYBR Green PCR Master Mix	Bio-rad	#1708880
ECL prime Western Blotting System	Santa cruz	Sc-2048
APO-BrdU TUNEL assay kit, with Alexa Fluor 488 Anti-BrdU	Thermo Scientific	A23210
Mouse Apoptosis Array Kit	R&D Systems	Cat ARY031
TruSeq mRNA Library Prep Kit	Illumina	20020595
TruSeq ChIP Sample Prep Kit	Illumina	IP-202-1012
Next Gem Single cell 3′ Reagent v3.1 kits	10x genomics	PN-1000123
Deposited data		
Raw and analyzed data	This paper	GEO: GSE216694
*Nrl*p-GFP;*Nrl*$^{-/-}$ mRNA-seq	Kim et al.[20]	GEO: GSE74660
Experimental models: Organisms/strains		
Mouse: C57BL/6	The Jackson Laboratory	https://www.jax.org/jax-mice-and-services/find-and-order-jax-mice
Mouse: *Kdm3b*$^{+/-}$	This paper	N/A
Oligonucleotides		
Primers for genotyping, common forward 5′-GGCACCAGACCCTGGGAGCTAG-3′	This paper	N/A
Primers for genotyping, WT reverse 5′-CACCCACGACCTGGCTTACACC-3′,	This paper	N/A
Primers for genotyping, KO reverse 5′-CACCCACGACCTGGCTTACACC-3′.	This paper	N/A
Primers for ChIP-seq validation, see Table S4	This paper	N/A
Software and algorithms		
TrimGalore (version 0.6.6)	Felix Kruger	https://github.com/FelixKrueger/TrimGalore
STAR (version 2.7.1a)	Dobin et al.[49]	https://github.com/alexdobin/STAR
RSEM (version 1.3.3)	Li and Dewey[50]	https://github.com/deweylab/RSEM
DESeq2 (version 1.32.0)	Love et al.[51]	https://bioconductor.org/packages/release/bioc/html/DESeq2.html
edgeR (version 3.36.0)	Robinson et al.[52]	https://bioconductor.org/packages/release/bioc/html/edgeR.html
Bowtie2 (version 2.4.4)	Langmead and Salzberg[53]	https://bowtie-bio.sourceforge.net/bowtie2/manual.shtml

(*Continued on next page*)

Continued

REAGENT or RESOURCE	SOURCE	IDENTIFIER
EPIC2 (version 0.0.41)	Stovner and Saetrom[54]	https://github.com/biocore-ntnu/epic2
HOMER (version 4.11.1)	Heinz et al.[55]	http://homer.ucsd.edu/homer/index.html
DAVID	Huang da et al.[56]	https://david.ncifcrf.gov/home.jsp
REVIGO	Supek et al.[57]	http://revigo.irb.hr/
GSEA (version 4.1.0)	Subramanian et al.[58]	https://www.gsea-msigdb.org/gsea/index.jsp
rMATs (version 4.1.2)	Shen et al.[59]	https://rnaseq-mats.sourceforge.net/
IRFinder (version 1.3.0)	Middleton et al.[60]	https://github.com/williamritchie/IRFinder
CellRanger (version 6.1.2)	10xGenomics	https://github.com/10XGenomics/cellranger
Scanpy (version 1.9.1)	Wolf et al.[61]	https://github.com/scverse/scanpy/
Velocyto (version 0.17.17)	La Manno et al.[26]	https://github.com/velocyto-team/velocyto.py
scVelo (version 0.2.4)	Bergen et al.[62]	https://github.com/theislab/scvelo
Samtools (version 1.15.1)	Danecek et al.[63]	http://www.htslib.org/
Bedtools (version 2.30.0)	Quinlan and Hall[64]	https://bedtools.readthedocs.io/
Python (version 3.9.13)	Python Software Foundation	https://www.python.org/
R (version 4.1.0)	The R foundation	https://cran.r-project.org/
IGV (version 2.8.7)	Robinson et al.[65]	https://software.broadinstitute.org/software/igv/
Cytoscape (version 3.9.1)	Cytoscape Consortium	https://cytoscape.org/
GraphPad Prism 8 (version 8.4.3)	GraphPad Software	https://www.graphpad.com/

RESOURCE AVAILABILITY

Lead contact

Further information and requests for resources should be directed to the lead contact, Prof. Jung-Woong Kim (jungkim@cau.ac.kr).

Materials availability

All unique reagents generated in this study are available from the lead contact without restriction or require a completed Materials Transfer Agreement if there is potential for commercial application.

Data and code availability

- Raw and processed RNA-Seq (Figure 1), scRNA-seq (Figures 2 and 5) and ChIP-Seq (Figures 3 and 4) data have been deposited in the Gene Expression Omnibus (GEO) database under accession number GSE216694 (https://www.ncbi.nlm.nih.gov/geo/query/acc.cgi?acc=GSE216694) and are publicly available as of the date of publication. The mouse RNA-Seq (Nrlp-GFP;Nrl-/- mRNA-seq) is available at GEO Accession number GSE74660.
- This paper does not report original code.
- Any additional information required to reanalyze the data reported in this paper is available from the lead contact upon request.

EXPERIMENTAL MODEL AND STUDY PARTICIPANT DETAILS

Expression strains

Kdm3b$^{+/-}$ mice was made by gene trapping system using pGT0lxf plasmid inserted between 12 and 13 exons of *Kdm3b* gene. Genotyping of *Kdm3b*$^{+/-}$ mice genotype was confirmed by PCR using genotyping primers; common forward 5′-GGC ACC AGA CCC TGG GAG CTA G-3′, WT reverse 5′-CAC CCA CGA CCT GGC TTA CAC C-3′, KO reverse 5′-CAC CCA CGA CCT GGC TTA CAC C-3′. Mice are maintained in a 12 hr light-dark cycle (light off on at 20:00) with free access to water and mice feed. Mice were weaned at 3 weeks-aged and housing 1-6 per cage. Mice were approved by the Institutional Review Board of Chung-Ang University (updated IRB number: 2019-00059 and 2020-00061).

METHOD DETAILS

Immunohistochemistry (IHC)

Kdm3b$^{+/-}$ mice retinas were excised quickly by removing the lenses on a cold plate within the PBS. After fixation with 4% paraformaldehyde (#15710; Electron Microscopy Sciences, Hatfield, PA, USA) of retinal tissues, samples were incubated in 10%, 20%, 30% sucrose-PBS for 1 hr, 3 hrs and 12 hrs, each. The fixed retina was embedded with 7% agarose gel or OCT compound (4583, SAKURA, CA, USA), retinas were

sectioned with vibratome (7000SMZ, Campden Instruments, England) and cryotome (CM1850, Leica, Germany), respectively. After permeabilize in PBS with 0.1% Triton X-100 for 10 min, sections were incubated for 1 hr in the blocking solution which including 5% normal goat serum in PBS with 0.1% Triton X-100. Primary antibodies were incubated for overnight at 4°C. Secondary antibodies incubated for 1 hr at 23-25°C in the dark condition after washed with PBS. The list of antibodies was described in Table S2. The nucleus was counterstained with 5 μg/ml 4′, 6-diamidino-2-phenylindole (DAPI) for 3 min in the dark. Fluorescence images were generated with Zeiss Axio Observer Z1 LSM 700 confocal microscope and ZEN program (ZEN lite 2011) (Carl zeiss, Oberkochen, Germany).

Retinal dissection and dissociation

Eyes were enucleated from animals and retinas dissected in fresh and cold 1X PBS. Dissected retinas were transferred to 1 ml of accutase per retina and incubated at 37°C for 20 min at shaking heat block (1,000 rpm), with gentle pipetting performed every 10 minutes. Dissociated retina cells were filtered out using 30 μm cell strainer (Miltenyi biotech, cat no. 130-098-458), and washed 2 times with cold $Ca2^{+}$ and $Mg2^{+}$ free 0.04 % BSA/PBS at 300 g for 5 min at 4°C. After the final centrifugation, supernatant was removed, and dead cells were removed from cells using Dead cells removal kit (Miltenyi biotech, cat no. 130-090-101) and MS columns (Miltenyi biotech, cat no. 130-042-201) according to the manufacture's protocol. Then, the collected live cells were gently resuspended in 1ml of ice cold 0.04 % BSA/PBS and counted with a LUNA-FX7™ Automated Fluorescence Cell Counter (logos Biosystems).

Single cell library preparation

According to the 10x Chromium Single Cell 3′ v3.1 protocol (10x Genomics, document no. CG000315) scRNA-seq libraries were prepared using the 10x Chromium controller and Next Gem Single cell 3′ Reagent v3.1 kits (10x genomics, PN-1000123) (ROKIT GENOMICS Inc.). Briefly, the cell suspension (target recovery 10,000 cells) was mixed with reverse transcription master mix and loaded with Single Cell 3′ Gel Beads and Partitioning Oil into a Single Cell G Chip (10x genomics, PN-1000120) to generate single-cell Gel Bead-in-emulsion (GEM). Poly-adenylated mRNA from single cells were uniquely barcoded and reverse-transcribed within GEM. After barcoded full-length cDNA was generated from mRNA through GEM-RT incubation, the barcoded cDNA molecules were amplified with PCR. For 3′ Gene Expression Library construction, the enriched cDNA was sequentially subjected to the enzymatic fragmentation, end-repair, A-tailing, adaptor ligation and index PCR.

Single-cell RNA sequencing (scRNA-seq)

The purified libraries were quantified using qPCR according to the qPCR Quantification Protocol Guide (KAPA) and qualified using the Agilent Technologies 4200 TapeStation (Agilent technologies). The library was sequenced using HiSeqXten platform (Illumina), and 150 bp paired-end reads were generated. The sequencing depth of 3′ Gene expression library was about 20,000 read pairs per cell.

Bioinformatics processing for scRNA-seq analysis

Sequencing output was processed through the Cell Ranger 6.1.2 mkfastq[66] and count pipelines using default parameters. To generate read count matrices from the fastq files, we used Cell Ranger count, which uses the STAR aligner[49] and mapped to the GRCm38 genome assembly. For the preprocessing of sequenced data, we calculated counts using the Cell Ranger pipeline and filtered using the Scanpy package.[61] To obtain spliced and unspliced read counts, we use Velocyto 0.17.17 command line tools with default parameter.[49] In the data preprocessing, we use Scanpy 1.9.1 to filter the spliced and unspliced matrix[61] for each sample. Quality control was performed in multiple steps. First, we remove all mitochondria and unknown gene. Second, we except the cell that has less than 200 genes and remove the gene that present in less than 3 cells from the analysis. Third, we use the Scrublet 0.2.3 to detect and remove doublets using default parameter.[67] Fourth, normalization and log transform were used to perform an additional cell-cell normalization. Finally, we used MAGIC 3.0. for imputing expected missing values and restoring the structure of data with knn=5 and t = 'auto'.[68] After these preprocessing processes, we calculate mRNA velocity for each sample using Velocyto 0.17.17 and scVelo 0.2.4 with default parameter.[26,62]

Clustering analysis and final cell type assignment

To investigate whether cells were consistent across the entire samples, we used the Batch balanced KNN (BB *k* NN) batch-alignment algorithm to correct bath effect with default parameter in Scanpy.[22] We also perform the normalization and filtering process as mentioned in the previous section. After preprocessing process, we apply the Louvain algorithm-based clustering was then performed to generate cell clusters, and clustering results were visualized using t-SNE. Major cell classes were manually annotated based on the cell maker genes.

Estimating mRNA stability in cells

mRNA stability was measured essentially as previously described.[26] The python package 'Velocyto' and scVelo were used for mRNA-stability analysis, which could estimate the mRNA stability in cells through quantifying the differences between the unspliced and spliced mRNAs. All analyses and results are obtained using default parameters and default data preparation procedures. The count matrices are size normalized to the median of total molecules across cells. Genes are selected out of those that pass a minimum threshold of 20 expressed counts commonly for spliced and unspliced mRNA. A nearest-neighbor graph (with 30 neighbors) was calculated based on Euclidean distances in principal component analysis space (with 30 principal components) on logarithmized spliced counts. For velocity estimation, first- and

second- order moments (means and uncentered variances) are computed for each cell across its 30 nearest neighbors. These are the default procedures in scVelo. We applied the same methods for each individual cell group to calculate velocity. To evaluate mRNA stability between the specific cell type relative to others, we calculated the difference of velocity γ as $\Delta(\gamma_{cell\ i} - \gamma_{ave.others})$ for cell type *i*. In scRNA-seq, cell counts vary among difference for cell types, potentially introducing bias in calculated $\gamma_{ave.others}$ for other cell types. To mitigate this bias, we individually computed velocities for each cell type and derived $\gamma_{ave.others}$ as the average γ across other cell types serving, as a representative measure for other cell types.

Immunoprecipitation and immunoblot

The retina tissues were lysed in a buffer containing 1% Triton X-100, 150 mM NaCl, 50 mM Tris-HCl, pH 7.5, 0.1% sodium dodecyl sulfate (SDS), 1% Nonidet P-40, and 1 mM PMSF. The cell suspensions from retina tissue were homogenized on the ice and centrifuged at 15,000 *g* at 4°C for 10 min. For immunoprecipitation assays, the supernatants were precleaned with 20 μl of protein A/G magnetic agarose beads (50% slurry) for 1 hr at 4°C and then incubated at 4°C overnight with 40 μl of protein A/G magnetic agarose beads in the presence of appropriate antibodies. The beads were washed 3 times in PBS, resuspended in 2X SDS sample buffer, and boiled for 10 min. The protein samples from the retina were electrophoresed on a 10% SDS-PAGE and transferred to a nitrocellulose membrane (Protran™; Whatman, Maidstone, UK). The membrane was blocked with 5% skim milk in TBST buffer (137 mM NaCl, 20 mM Tris–HCl, pH 7.6 and 0.1% Tween-20), and incubated with suitable diluted primary antibody for overnight at 4°C. The list of antibodies was described in Table S2. Membranes were washed three times for 10 min with TBST and incubated with a 1:5000 dilution of horseradish peroxidase-conjugated anti-mouse or anti-rabbit antibodies for 1 hr. Blots were washed with TBST three times and developed with the Western blotting luminol reagent (sc-2048, Santa Cruz) according to the manufacturer's protocols.

AAV viral vector production and subretinal injection

AAV viral vectors used to overexpress or knockdowned the *Kdm3b* or the GFP control were constructed and packaged into AAV2.7m8 by Vector Builder (Chicago, USA). A single batch of AAV2.7m8 vectors was generated for this study, tittered at 2.7 to 3.93 × 10^{11} GC/ml, stored in aliquots at −80°C, and thawed as needed for all experiments in this study to avoid freeze-thawing or potential variations in viral titer. To exclude batch effect by biological individual difference, we injected each control and overexpression or knock down AAV constructs simultaneously to the same mouse. We injected 2 μl of control AAV (p*CMV*-GFP: 2.7 × 10^{11} GC/ml, p*U6*-shScramble-GFP: 3.87× 10^{11} GC/ml) and overexpression or knockdown AAV (p*CMV-Kdm3b*-T2A-GFP: 2.06 × 10^{11} GC/ml, p*U6-shKdm3b*-GFP: 3.93 × 10^{11} GC/ml) in subretinal region of left and right eyes, respectively. Two weeks after, the retinas were collected separately for IHC.

Total RNA isolation and RT-qPCR

Total RNA was extracted using the TRIzol solution (15596018, Invitrogen, CA, USA) by the manufacture's specifications. Contaminated genomic DNA was removed from 10 μg of total RNA by the incubation with 20 units of RNase-free DNase I (New England Biolabs) and 4 units of RNase inhibitor (New England Biolabs) in DEPC-treated water. The reaction mix was incubated for 1 hr at 37°C and then for 10 min at 50°C. The RNA samples quantified spectrophotometrically at 260 nm and all RNA extracts had an OD260:OD280 between 1.8 and 2.0, demonstrating that RNA was extracted clearly. Oligo-dT (6110A, Takara) was applied as the primer in the first step of cDNA synthesis. Total RNA (1 μg) was combined with 1 μl of oligo dT, and H_2O and then preheated at 70°C for 10 min to denature the secondary structures of RNA. The mix was then cooled off quickly to 4°C, subsequent to which 10 mM DTT, 2 μl of 10X reverse-transcriptase buffer, and 200 units of reverse transcriptase (18064022, Invitrogen, CA, USA) was added to make a total volume of 20 μl. The reverse-transcriptase mixture was incubated at 40°C for 60 min, after which it was stopped by heating at 94°C for 20 sec. The cDNA stock was stored at -20°C. The specificity of each of the amplified products was proved by melting curve analysis. For real-Time quantitative PCR, the iQ SYBR Green PCR Supermix (#1708880, Bio-Rad) and the CFX96 Real-time PCR detection system (Bio-Rad) were applied to detect amplified cDNA samples by the manufacturer's instructions. The β-actin gene was applied for normalization. The relative mRNA expression was calculated by the $2^{-(\Delta\Delta Ct)}$ method.

Electroretinogram (ERG)

Mice were given full field flash ERG to assess retinal function in response under scotopic and photopic conditions.[69] Mice were dark adapted overnight for scotopic measurements after anaesthetized with 2X avertin solution (200 μl per 20 g mouse) with tribromoethanol (T48402, SIGMA) and tert-amyl alcohol (240486, SIGMA). Pupils are dilated with isopto atropine (Alcon, Republic of Korea), and add a small drop of 1% hypromellose (Samil, Republic of Korea) to each eye prior to recordings. Ground and reference subdermal electrodes were placed subcutaneously near the hindquarter and between the eyes respectively and the mouse placed on a heated pad (37°C). Recording electrodes were placed on the cornea, ERG was carried out under scotopic conditions for both eyes simultaneously, with increasing green light stimulus strengths. After mice are adapted to 1.6 log cd·sec/m^2 for 5 min, the photopic responses are recorded.

Transmission electron microscopic (TEM) analyses

The enucleated retinas were fixed in 4% paraformaldehyde (Alfa Aesar, USA) dissolved in 1X PBS for overnight at 4°C. After fixation, retina tissues were washed with 0.1M sodium cacodylate buffer, pH7.2, and postfixed with 1% osmium tetroxide (OsO4) in 0.1M PBS for 1 hr at 4°C. The retinas dehydrated in an ethanol gradient to 100% and embedded in Durcupan™ resin (Sigma-Aldrich, USA). The blocks cut into ultrathin

sections, stained with 2% uranyl acetate and 4% lead citrate, and mounted on gold grids. The retinas photographed with a Transmission electron microscopy (Tecnai F20 G2, FEI). Sections were scanned randomly at < 30 kV.

RNA sequencing and bioinformatical analysis

RNA-seq library was generated by TruSeq mRNA Library Prep Kit (Illumina, Inc., USA) by the manufacturer's instructions. To be brief, each 100 ng total RNA from pooled retinas (>4 retinas) were isolated and an oligo-dT primer including an Illumina-compatible sequence at its 5′ end was hybridized to the RNA and reverse transcription was carried out. After degradation of the RNA template, second strand synthesis was initiated by a random primer containing an Illumina-compatible linker sequence at its 5′ end. The double-stranded library was purified by employing AMPure magnetic beads (A63881, Beckman coulter, CA, USA) to get rid of all reaction components. The library was amplified to add the complete adapter sequences required for cluster generation. The finished library is purified from PCR components. High-throughput sequencing was carried out as paired-end 101 sequencing reads using NovaSeq 6000 and HiSeq 2500 (Illumina, Inc., USA). mRNA-Seq reads were aligned using STAR-2.7.1a (Table S3). Indices were either produced from GRCm38.p13.101 genome assembly sequence or the representative transcript sequences for aligning to the genome and transcriptome. The alignment file was applied for assembling transcripts, estimating their abundances and detecting differential expression of genes. We perform read feature counting with RSEM (v.1.3.3) and FPKM were calculated using a FPKM function from DESeq2 (v.1.32.0) and differential gene expression by edgeR (v.3.36.0) using R package.

Chromatin immunoprecipitation (ChIP) sequencing

Retina tissue samples (pooled for each sample, at least 16 retinas at P60) were cross-linked by 1% paraformaldehyde for 10 min at 23°C, and glycine was added to quench the reaction at a final concentration of 125 mM. The samples were homogenized in SDS lysis buffer (1% SDS, 10 mM EDTA, and 50 mM Tris-HCl, pH 8.1), and chromatin was then sheared by bioruptor sonicator (Diagenode) for 40 cycles (30 s on / 30 s off, repeat 2 times) at high power setting. After centrifugation for 10 min at 18,500 *g*, samples were resuspended in ChIP dilution buffer (0.01% SDS, 1.2 mM EDTA, 1.1% Triton X-100, 167 mM NaCl, and 16.7 mM Tris-HCl, pH 8.1). The sonicated lysates were subjected to immunoprecipitation using the indicated antibodies (5 μg of antibodies for each immunoprecipitation (IP) reaction) for overnight. Protein A/G magnetic beads (26162, Thermo scientific, USA) (30 μl) were added, and immunoprecipitations were continued for an additional 4 h, and washed with low-salt wash buffer (0.1% SDS, 1% Triton X-100, 2 mM EDTA, 150 mM NaCl, 20 mM Tris-HCl, pH 8.1), high-salt wash buffer (0.1% SDS, 1% Triton X-100, 2 mM EDTA, 500 mM NaCl, 20 mM Tris-HCl, pH 8.1), LiCl immune-wash buffer (0.25 M LiCl, 1% NP40, 1% deoxycholate, 1 mM EDTA, 10 mM Tris-HCl, pH 8.1), and Tris-EDTA buffer (1 mM EDTA, 10 mM Tris-HCl, pH 8.0). Following the final wash, immunoprecipitates were eluted with 100 μl of IP elution buffer (1% SDS, 0.1 M $NaHCO_3$) twice and reverse crosslinked at 65°C for overnight. DNA/protein complexes were precipitated with 100% ethanol, air-dried, and dissolved in 20 μl of distilled water (W4502, Sigma). The list of primer for validation of ChIP-seq was described in Table S4.

ChIP-seq library preparation and bioinformatical analysis

ChIP-seq library was generated by TruSeq ChIP Library Preparation Kit (Set A, IP-202-1012, Set B, IP-202-1024, Illumina, CA, USA) by the manufacturer's instructions. To be brief, 5 μg of input and ChIP-enriched DNA were end-repaired, A-tailing, and adapter ligation with TruSeq index adapters, and amplified. Paired-end sequencing of all ChIP libraries was performed on the Illumina NextSeq 500 platform. c-Fos and inputs ChIP-seq fastq in mouse cortical neurons were downloaded from the GEO (GSE60192).[70] For processing of KDM3B and histone modification ChIP-seq in the retina, all ChIP reads in FASTQ format were aligned to the GRCm38.p13.101 mouse genome using Bowtie2 (ver 2.4.4) and removed redundant reads Table S4. Peak calling was performed with EPIC2 (ver 0.0.41) with the default parameters: bin size = 200; fragment size = 150; Gap allowed = 3, FDR cutoff < 0.05). After confirmed the consistency between each replicate, we pooled extended reads and generated the bigwig track for visualization with IGV (ver.2.8.7).

Motif discovery

Overrepresented motif analysis of sequences enriched under KDM3B ChIP-seq peaks was performed using the *de novo* motif finder MEME-ChIP [http://meme.nbcr.net/meme/tools/meme-chip, date last accessed, July 2015]. A 300 bp sequence surrounding each of the ChIP-Seq peak summits (extending 150 bp on each side) was supplied to MEME-ChIP as input and analyzed with default settings for motif width and significance thresholds. For transcription factors with several motifs, a correlation score between the motifs was calculated using HOMER 4.11.1.[55]

Gene ontology and GSEA analysis

DAVID (http://david.abcc.ncifcrf.gov) allowed significant DEGs and ChIP-seq peaks in respective gene sets to be clustered into functional gene ontologies. Enriched gene ontology terms were identified using Metascape, and scatter plots of ontology terms were made using REVIGO.[71] GSEA analysis was performed using (GSEA 4.1.0; http://www.broadinstitute.org/gsea/index.jsp) with MsigDB v7.1 mouse database.

Epigenomic network construction

KDM3B-centered network was constructed by integrating between RNA-seq and ChIP-Seq data analysis as follows. First, the nearest neighbor (NN) genes for KDM3B were selected by filtering condition (ChIP-count > 10 per each gene). Next, 2nd NN genes of KDM3B

were performed using NetworkAnalyst.[72] The selected 2nd NN gene linked with 1st NN gene. All networks were considered by 3rd NN. For all candidate genes of network, genes from RNA-Seq were filtered by FPKM > 10. For measurement of network robustness, we compared the impact of random link removal on the KDM3B-centered networks between *Kdm3b*$^{+/+}$ (6, 12, and 18 months) and *Kdm3b*$^{+/-}$ (12 months) mice.

Measurement of network structural dissimilarities

Network dissimilarity measurement was done following the approach proposed by Shieber et al.[36] This method compared network structures based on quantifying differences among distance distributions, node dispersion metric and α-centrality.

$$D(G,G') = w_1\sqrt{\frac{J(\mu_G,\mu_{G'})}{\log 2}} + w_2\left|\sqrt{NND(G)} - \sqrt{NND(G')}\right| + \frac{w_3}{2}\left(\sqrt{\frac{J(P_{\alpha G},P_{\alpha G'})}{\log 2}} + \sqrt{\frac{J(P_{\alpha G^c},P_{\alpha G^{c'}})}{\log 2}}\right)$$

Here, J represents Jensen-Shannon divergence. The first term represents dissimilarity in average node connectivity μ_G is the graphs averaged node-distance distribution. The second term shows dissimilarity in a node dispersion metric ($NND(G)$). And the last term denotes difference for distribution of α-centrality ($P_{\alpha G}, P_{\alpha G^{c'}}$) that measures the influence of a node in the given graph G and its complement graph (G^c). We measured network dissimilarity following the algorithm,[36] using $w_1 = 0.45$, $w_2 = 0.45$, $w_3 = 0.1$ values.

QUANTIFICATION AND STATISTICAL ANALYSIS

Image analysis

The number of nuclei in ONL was counted on the middle of the *Kdm3b*$^{+/+}$ and *Kdm3b*$^{+/-}$ mice retina. The thickness of ONL was measured by using 'length measurement' plugin of ImageJ software. The number of cone photoreceptor was counted on the middle of *Kdm3b*$^{+/-}$ mice inferior retina. Size of cone photoreceptor synapse was measured by using 'area measurement' plugin ImageJ software. Intensities of GFAP and Cytochrome c were measured by using 'histogram' plugin ImageJ software. Especially, the intensity of Cytochrome c released was measured within each cell's cytoplasm by using 'automated measurement' plugin NIS software. The 3D reconstruction image was generated using Oxford Bitplane Imaris (ver 9.3.1, Bitplane, CT, USA). The quantity of vesicles attached to rod spherules and cone pedicles was assessed through the analysis of transmission electron microscopy (TEM) images. The count of vesicles in close proximity (~0.05 μm) to the rod and cone ribbons was conducted, and the number of vesicles not attached to the ribbon was tallied within a single rod spherule and cone pedicle.

Statistical analysis

A statistic software, GraphPad PRISM was used to examine the significance of differences between result data with independent two-sample t-test. The results were described by mean ± standard error of the mean (SEM) and gained from two or three separated experiments. P values less than 0.05 were considered statically significant.